MOUNTAIN-PLAINS CONSORTIUM

MPC 22-490 | Y. J. Kim

REPAIRING CONCRETE STRUCTURES USING NEAR-SURFACE MOUNTED COMPOSITES WITH INORGANIC RESINS UNDER SIMULATED MULTI-HAZARD DAMAGE

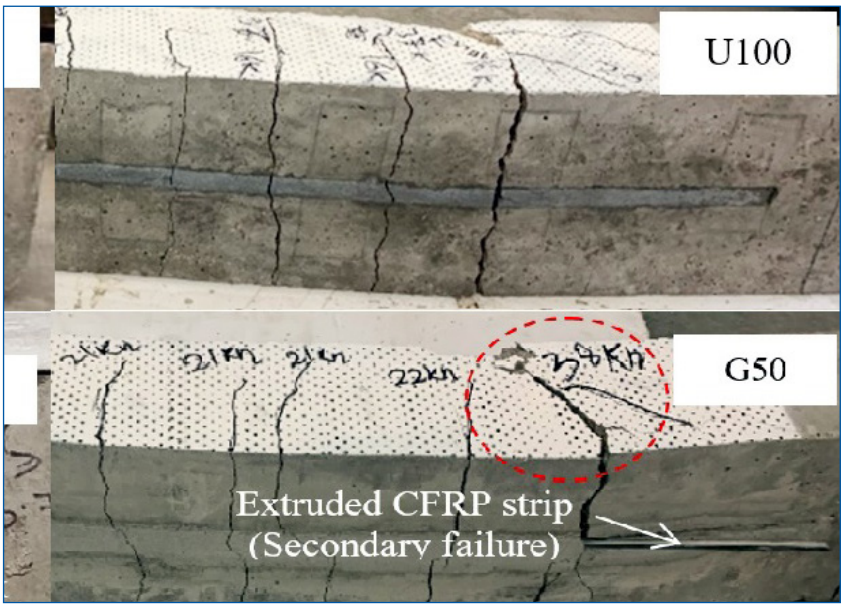

MOUNTAIN-PLAINS CONSORTIUM REGION 8

A University Transportation Center sponsored by the U.S. Department of Transportation serving the Mountain-Plains Region. Consortium members:

Colorado State University
North Dakota State University
South Dakota State University
University of Colorado Denver
University of Denver
University of Utah
Utah State University
University of Wyoming

Technical Report Documentation Page

1. Report No.	2. Government Accession No.	3. Recipient's Catalog No.
MPC-648		

4. Title and Subtitle	5. Report Date
Repairing Concrete Structures Using Near-Surface Mounted Composites with Inorganic Resins under Simulated Multi-hazard Damage	December 2022
	6. Performing Organization Code

7. Author(s)	8. Performing Organization Report No.
Yail Jimmy Kim, PhD, PE, FACI	MPC 22-490

9. Performing Organization Name and Address	10. Work Unit No. (TRAIS)
University of Colorado Denver 1200 Larimer Street Denver, CO, 80217	11. Contract or Grant No.

12. Sponsoring Agency Name and Address	13. Type of Report and Period Covered
Mountain-Plains Consortium North Dakota State University PO Box 6050, Fargo, ND 58108	Final Report
	14. Sponsoring Agency Code

15. Supplementary Notes

Supported by a grant from the US DOT, University Transportation Centers Program

16. Abstract

The first part of the study presents the time-dependent interfacial behavior of near-surface-mounted (NSM) carbon fiber reinforced polymer (CFRP) strips bonded to a concrete substrate using inorganic resins. Four types of bonding agents (mortar, polyestersilica, ultra-high performance concrete (UHPC), and geopolymer) are tested to appraise the potential for NSM application with a focus on rheological and mechanical performance during a curing period of 28 days. The second part of the study discusses the feasibility and relevance of cementitious resins as a bonding agent for NSM CFRP strips. Contrary to conventional organic matrices, such inorganic resins offer promising performance when subjected to aggressive environments, especially under thermal distress. Three emerging resins are employed (polyester-silica, UHPC, and geopolymer) to strengthen reinforced concrete beams alongside NSM CFRP. After stochastically simulating various levels of pitting corrosion for a period of 100 years, the outcomes are represented in the beams by reducing the cross-sectional area of steel reinforcement before applying the rehabilitation system. The emphasis of experimental investigations lies on the workability of those resins and the flexural response of the retrofitted beams. Material-level testing reveals that the rheological properties of the resins are not related to their compressive strength. As far as loadcarrying capacity is concerned, the beams bonded with polyestersilica outperform the beams with other resins; however, UHPC enables stable degradation over the years.

17. Key Word	18. Distribution Statement
composite materials, concrete structures, guidelines, repairing, resins	Public distribution

19. Security Classif. (of this report)	20. Security Classif. (of this page)	21. No. of Pages	22. Price
Unclassified	Unclassified	68	n/a

Form DOT F 1700.7 (8-72) Reproduction of completed page authorized

Repairing Concrete Structures Using Near-Surface Mounted Composites with Inorganic Resins under Simulated Multi-hazard Damage

Yail Jimmy Kim, Ph.D., P.Eng., FACI

Department of Civil Engineering
University of Colorado Denver
Denver, Colorado

December 2022

Acknowledgments

The principal investigator gratefully acknowledges all individuals who contributed to the present research report.

Disclaimer

The contents of this report reflect the work of the author, who is responsible for the facts and the accuracy of the information presented. This document is disseminated under the sponsorship of the Mountain-Plains Consortium in the interest of information exchange. The U.S. Government assumes no liability for the contents or use thereof.

EXECUTIVE SUMMARY

The first part of the study presents the time-dependent interfacial behavior of near-surface-mounted (NSM) carbon fiber reinforced polymer (CFRP) strips bonded to a concrete substrate using inorganic resins. Four types of bonding agents (mortar, polyester-silica, ultra-high performance concrete (UHPC), and geopolymer) are tested to appraise the potential for NSM applications with a focus on rheological and mechanical performance during a curing period of 28 days. Unlike mortar and geopolymer resin cases, the rheological resistance of the polyester-silica and UHPC resins increases within 30 minutes owing to an evolved setting process. The hydration of mortar continues for up to 28 days of curing in line with assorted chemical reactions. The compressive strength of polyester-silica gradually ascends to 35 MPa (5,076 psi) at 28 days, while that of UHPC rapidly rises to 95.3 MPa (13,822 psi) at three days. Contrary to the stabilized interfacial capacity of the specimens with mortar and geopolymer after seven days, the capacity of the specimens with polyester-silica steadily develops until 28 days. Unlike the failure mode of other cases over time, a shift in the plane of failure is noticed for the mortar-bonded interface. The post-peak response and energy dissipation of the interface are controlled by the resin type and curing period. Analytical modeling quantifies the level of hazard and clarifies the functional equivalence of the interface with the inorganic resins against conventional organic epoxy resins.

The second part of the study discusses the feasibility and relevance of cementitious resins as a bonding agent for NSM CFRP strips. Contrary to conventional organic matrices, such inorganic resins offer promising performance when subjected to aggressive environments, especially under thermal distress. Three emerging resins are employed (polyester-silica, UHPC, and geopolymer) to strengthen reinforced concrete beams alongside NSM CFRP. After stochastically simulating various levels of pitting corrosion for a period of 100 years, the outcomes are represented in the beams by reducing the cross-sectional area of steel reinforcement before applying the rehabilitation system. The emphasis of experimental investigations lies in the workability of those resins and the flexural response of the retrofitted beams. Material-level testing reveals that the rheological properties of the resins are not related to their compressive strength. Regarding load-carrying capacity, the beams bonded with polyester-silica outperform the beams with other resins; however, UHPC enables stable degradation over the years. The interfacial characteristics of the resins dominate the mechanical interaction between the damaged internal reinforcing steel and CFRP, thereby altering the tendency of capacity drops, post-yield plateaus, and crack distributions. Through analytical modeling, the provisions of existing design guidelines are evaluated, and a modification factor is suggested to promote the cementitious resins for NSM CFRP.

TABLE OF CONTENTS

PART I: Time-Dependent Bond of Concrete and NSM CFRP with Inorganic Resins

PART II. Cementitious Resins for Strengthening RC Beams with NSM CFRP

LIST OF TABLES

[PART I]

[PART II]

LIST OF FIGURES

[PART I]

[PART II]

PART I: TIME-DEPENDENT BOND OF CONCRETE AND NSM CFRP WITH INORGANIC RESINS

1. INTRODUCTION

The sustainability of built-environments is a pressing demand in modern society owing to the aging, deterioration, and impairment of structural systems. In lieu of costly reconstruction, rehabilitation is preferred to upgrade the capacity and serviceability of load-carrying elements. Structural strengthening is an efficient technique to extend the lifespan of existing concrete members affordably. Traditional approaches involve placing steel plates, enlarging cross sections, adding supplementary beams, and post-tensioning with external cables (Taljsten and Blanksvard 2007; ACI 2017). While effective, these methods offer temporary solutions and require significant labor, specialized equipment, and follow-up maintenance. Carbon fiber reinforced polymer (CFRP) is deemed a viable option to reconstitute and modify structural conditions in buildings and bridges (ACI 2017). Typically, CFRP is either directly bonded to the tensile side of concrete (externally bonded [EB]) or inserted into a precut groove (near-surface-mounted [NSM]) for strengthening constructed members (ACI 2007). Compared with the EB method, the NSM method offers notable advantages: superior bond, durability, aesthetics, and insusceptibility to surface quality (De Lorenzis and Teng 2007). Epoxy adhesives are predominantly employed for bonding NSM CFRP strips; however, several drawbacks were reported: degraded functionality under thermal distress, exothermic reactions, noxious fumes, and incompatibility with wet exteriors (Taljsten and Blanksvard 2007; Hashemi and Al-Mahaidi 2012). To address these concerns, inorganic resins can be considered as an alternative and research is actively underway (Yu et al. 2021).

Inorganic resins are particularly beneficial when CFRP-installed members are subjected to aggressive environments, such as elevated temperatures, ultraviolet rays, and detrimental chemicals (Vasconcelos et al. 2011; Al-Jaberi et al. 2019). Assorted compositions in a mixture affect the performance of inorganic resins. For instance, the presence of silica fume changes the microstructure of a resin by filling voids and reducing porosity (Ahmad and Chen 2020). Mortar is a widely known inorganic resin, and other contemporary materials may be suitable for NSM CFRP systems. Polyester is mostly composed of propylene glycol, maleic anhydride, and phthalic anhydride (Evans et al. 1996) and retains a crosslinking architecture for adequate engineering properties (Mandredi et al. 2006). Polyester resins may be blended with silica sand to intensify mechanical resistance (Chokrieh et al. 2015). Ultra-high performance concrete (UHPC) is a state-of-the-art composite comprising cement, water, silica fume, sand, a high-range water reducer, and other admixtures (ACI 2018). The optimally graded granular constituents of UHPC increase packing density at a water-cement ratio of less than $w/c = 0.25$ (Graybeal 2014; Shi et al. 2021). The compressive strength of UHPC varies between 120 MPa (17.4 ksi) and 150 MPa (21.8 ksi) and its interfacial strength to a concrete substrate is over 20 MPa (2.9 ksi) (Graybeal 2014; CDOT 2018; Feng et al. 2020). Because UHPC does not contain coarse aggregate, it can be placed in a narrow space without restriction. Geopolymer is an environmentally friendly amorphous cementitious product with a low carbon footprint and provides favorable thermal stability (Vasconcelos et al. 2011). Other benefits include negligible shrinkage, prompt setting, durability, and acid resistance (Li et al. 2004; Wasim et al. 2021). Geopolymer is synthesized by the dissolution of aluminosilicates in an alkali solution, the reorientation of free ion clusters, and polycondensation (Li et al. 2004). Notwithstanding the applicability of these nonconventional resins, limited information is available on bond and anchorage for NSM CFRP (Yu et al. 2021).

This research deals with an experimental program examining the pertinence of emerging inorganic resins (polyester-silica, UHPC, and geopolymer) to NSM CFRP, and evaluates the behavior against that of mortar. Since inorganic resins generally need a long curing period relative to organic resins, progressive bond development is of interest. It should be noted that, for practical reasons, the majority of published research outcomes concerning NSM systems have focused on the performance of sufficiently cured resins (Al-Saadi et al. 2019). Attention is thus paid to the time-dependent material characteristics and load-bearing mechanisms of a CFRP-inorganic resin interface with an emphasis on rheology, strength, failure mode, and energy dissipation. Through theoretical modeling, functional equivalence between the organic and inorganic resins is measured and the hazard level of the inorganic resins is analyzed.

2. RESEARCH SIGNIFICANCE

In spite of known deficiencies, NSM CFRP technologies heavily rely on the use of organic epoxy resins. The rehabilitation community acknowledges the familiarity, efficacy, and customary adoption of such bonding agents; but also, practitioners are eager for a substitute that can overcome the limitations of epoxy adhesives under specific circumstances, as in the case of a temperature-sensitive environment. The provisions of ACI 440.2R-17 (ACI 2017) do not mention other resin types for NSM CFRP; therefore, an update is essential. Ongoing endeavors to handle these practical necessities are found in the utilization of inorganic resins. For strengthening application, inorganic resins should provide satisfactory mechanical properties, acceptable workability, and adaptability to a concrete substrate. The present study explores a new opportunity with promising inorganic resins and appraises their effectiveness and feasibility as part of an NSM system.

3. EXPERIMENTAL PROGRAM

Outlined in this section are materials constituting an NSM CFRP system with inorganic bonding agents, specimen preparation, and test approaches. The implications of various curing periods are emphasized to elucidate the early-age bond of the strengthening system.

3.1 Materials

Ready-mix concrete was used with a specified compressive strength of f'_c = 25 MPa (3,630 psi). Pursuant to ASTM C39 (ASTM 2018), five cylinders (100 mm [4 in.] in diameter and 200 mm [8 in.] in length) were tested at 28 days and an average strength of 27 MPa (3,920 psi) was obtained with a coefficient of variation of 0.013. Unidirectional CFRP strips (2 mm [0.08 in.] thick by 16 mm wide [0.63 in.]), consisting of carbon fibers and a bisphenol epoxy vinylester resin, had a nominal tensile strength of f_{fu} = 2,068 MPa (300 ksi) with an elastic modulus of E_f = 124 GPa (18,000 ksi), and a rupture strain of 1.7%. The surface of the strips was textured by the manufacturer to improve adhesion against a bonding agent [Figure I1(a)]. Four types of inorganic resins were employed: mortar, polyester-silica, UHPC, and geopolymer. The mortar was mixed with general-purpose Portland cement (Type I) and ordinary sand at a water-cement ratio of w/c = 0.5. To produce a polyester-silica resin, a viscous polyester liquid was promoted with a catalyst for chemical reactions and blended with silica sand (SiO_2 = 90.3%, particle size = 0.45 mm (0.018 in.), and specific gravity = 2.62) at a mass ratio of 18%, 2%, and 80%, respectively. The resin's setting time was 25 minutes. The UHPC grout was a non-shrink and particle-optimized product. Although details cannot be released due to proprietary reasons, the two-phase mixture was formulated with engineered carbon nano fibers and was flowable at 280 mm in accordance with ASTM C230 (ASTM 2021). The geopolymer resin, formed by the condensation of aluminosilicates, was a low porosity cementitious composite and its cohesion was accomplished by the covalent bond between tetravalent silicon and trivalent aluminum. The succeeding properties are reported by the manufacturer: chloride penetration = 60 mm (2.4 in.) at 90-day ponding (ASTM C1543, ASTM 2010), loss = 0% under 300 cycles of freeze-thaw (ASTM C666, ASTM 2015a), set time = 60 minutes (ASTM C807, ASTM 2020a), and shrinkage = 0.07% at 28 days (ASTM C1090, ASTM 2015b).

3.2 Specimens

Complying with ASTM C109 (ASTM 2020b), 50-mm (2-in.) cubes were prepared with the aforementioned inorganic resins and cured in an environmental chamber (a relative humidity of 99% at 23°C [73°F]). Figure I1(a) shows the schematic of a specimen for interface-testing, which consisted of a concrete prism (100 mm [4 in.] by 100 mm [4 in.] by 300 mm [12 in.]) and a precut CFRP strip of 275 mm (11 in.). Each prism was cast in a steel mold with a Styrofoam to secure a space for placing the strip. The size of grooves (13 mm [0.5 in.] wide by 25 mm [1 in.] deep) was determined by the recommendation of ACI 440.2R-17 (ACI 2017). After curing the prisms in the chamber for 28 days, the specimens were airbrushed to eliminate unnecessary residues, washed with tap water, and dried. The surfaces of the concrete were roughened utilizing a knotted-wire steel wheel to enhance the bond against the resins. The inorganic resins were poured in the cleaned groove and the CFRP strip was gently inserted. The loaded end of the prism was intentionally unbonded by 13 mm (0.5 in.) to avoid a stress concentration, and the total length of the bonded strip was 200 mm (8 in.).

3.3 Test Methods

The cylinders and cubes were monotonically loaded under axial compression [Figures I1(b) and (c), respectively]. Five cubes were replicated at 1, 3, 7, 14, and 28 days (100 cubes in total for the four resins) to establish the time-dependent strength gains of the inorganic bonding agents. The rheology of the fresh resins was assessed using a vane tester [Figure I1(d)] to monitor workability for NSM application. As guided by the instruction manual, plastic containers were filled with the resins and the vane shaft was rotated at 0.1 rpm (revolutions per minute) for a period of up to 60 minutes, which would be long enough to bond NSM CFRP in the field. The interface test specimens were positioned in a custom-made fixture and mounted to a universal testing machine [Figure I1(e)]. The gripped-end of the CFRP strip was tensioned against the fixed concrete prism until failure, and the load and displacement were recorded by a computerized data acquisition system. A total of 60 prisms were tested (Table I1); three specimens were repeated per curing period at the same intervals as the cubes.

4. TEST RESULTS

Experimental outcomes include the material and interfacial characteristics of inorganic resins for NSM CFRP. The rheology, strength, and bond of the resins are delineated in conjunction with load-carrying capacity, grade classification via statistical clustering, failure modes, and energy dissipation.

4.1 Rheology of Unhardened Resins

The rheological properties of the liquid-like resins were measured by (Bauer et al. 2007)

$$\tau = \frac{T}{\pi\left(\frac{D^2 H}{2} + \frac{D^3}{6}\right)} \tag{I1}$$

where τ is the shear stress regarding the flow of the fresh resin; T is the applied torque ($T = K\Delta\theta$, in which K is the spring constant (1.85 Nmm [0.016 lb-in.] per angular change) and $\Delta\theta$ is the angular change ($\Delta\theta$ = degrees/180); and D and H are the width and depth of the vane, respectively (D = 12.7 mm (0.5 in.) and H = 12.7 mm (0.5 in.). The shear stress of the polyester-silica resin ascended with time [Figure I2(a)]; scilicet, the rheological resistance of the resin, increased as it coagulated. The stress of UHPC was stationary until 30 minutes and began to grow; the resin stiffening was evidence of an initiated setting process. The mortar and geopolymer resins exhibited an insignificant increase in the shear stress. Generally, the setting time of mortar and geopolymer takes three to eight hours (Yim et al. 2017; Arnoult et al. 2019). Complying with the principle of Newtonian fluids (Ramsey 2019), the viscosity of the resins was calculated (i.e., the slope of a shear stress vs. strain rate relationship) and is provided in Figure I2(b). The low strain rates close to zero (< 0.0015 rad/sec.) corroborate that these resins were viscoelastic materials (Barnes et al. 1989). When the viscosity rose, the strain rate of the polyester-silica resin quickly declined owing to the entangled intermolecular friction in the polyester resin (Snijkers et al. 2015). The rate of UHPC also went down initially and tended to plateau over a viscosity of 247 kPa-s/rad. (35.8 psi-s/rad.). The logged strain rates of the mortar and geopolymer resins were practically in a steady state at an average of 0.0002 rad./sec.

4.2 Strength of Inorganic Resins

Time-dependent variation—Figure I3 exhibits the strength development of the inorganic resins. For the purpose of comparison, the ordinate of the graphs was maintained in a single scale (close-up views were added for those that possessed relatively low strengths). As the hydration of the mortar became active [Figure I3(a)], the cement paste set in a day from casting at an average strength of 4.7 MPa (682 psi). Hydrated calcium silicates are known to be the source of cohesion in the binder (Jonsson et al. 2005) and the cohesive substance enabled strength gains in the mixture. Meanwhile, crystallized calcium hydroxide formed with capillary and gel pores (Hlavacek et al. 2018). It should be noted that, unlike capillary pores, the creation of gel pores is not a function of water-cement ratio and continued hydration (Neville 1995). The gradual strength growth up to 28 days implies that the amount of free water in the capillaries decreased over time and thus the chemical reactions for hydration became slow (Tang et al. 2017). The compressive strength of the polyester-silica resin rose in a manner similar to that of the mortar resin, as shown in Figure I3(b), whereas the average strength of the former was 64.2% higher at 28 days. During a curing process, the thermosetting polymeric resin with condensation reactions generated a set of cross-linked monomers alongside a free radical flux (Vargas et al. 2012). The progressive hardening of the resin was accomplished by molecular gelation and vitrification (Jankovic 2010). The weak link of the composite resin was the contact between the polyester matrix and silica particles (Erofeev et al. 2020),

which will be revisited when the failure mode of the interface-test specimens is discussed. The early-age strength of UHPC was remarkable at an average of 61.9 MPa (8,978 psi) and 95.3 MPa (13,822 psi) for one- and three-day curing periods, respectively [Figure I3(c)]. The fact that the amount of C_3S and the fineness of binders are responsible for the rate of a strength increase in cementitious composites (Neville 1995) explains the attributes of the commercial product entailing rapid hydration reactions. The fine size of the binder particles (inappropriate to disclose because of a contractual obligation) is expected to reduce bond stresses inside the mixture (Costa et al. 2017), which led to an average strength of 120 MPa (17,400 psi) at 28 days. On average, despite the visual similarity of the cured cubes [Figs. I3(a) and (d), insets], the one-day strength of geopolymer [7.8 MPa (1,131 psi), Figure I3(d)] was 39.1% higher than that of the mortar, and their discrepancy enlarged up to 48.6% at 28 days. The noticeable compressive strength of the geopolymer resin was achieved through the dissolution of aluminum and silicon as well as through polycondensation with metallic elements such as Fe, Ca, and Mg in natural minerals (Xu and Van Deventer 2000). Crystallographic analysis based on X-ray diffraction (XRD) clarifies the formation of tetrahedral silicon in the alumonosilicate geopolymer and the creation of calcium silicate hydrate in the conventional mortar (Tailby and MacKenzie 2010).

Characteristic response—The average strength of the resins is summarized in Figure I4(a). The one-day strength of mortar was the lowest and that of UHPC was the highest. Such a propensity was preserved up to 28 days. As visible in the normalized strength showing a fractional increment [Figure I4(b)], the compressive resistance of the mortar resin was positively correlated with time and the dependency was strong (linear slope). The logarithmic-shape illustration of other resins substantiates that the portion of the early-age strength was considerable, and the degree of curvature can be a characteristic feature for each resin. The strength development rate of all resins was distinguishable before seven days of curing [Figure I4(b), inset], during which the rate of UHPC was prominent and those of the polyester-silica and geopolymer resins were close.

4.3 Interfacial Capacity

Trend analysis—The ultimate load of the CFRP-concrete interface is plotted in Figure I5. The interfacial capacity of the mortar-bonded specimens steadily increased and stabilized [Figure I5(a)]. For example, on average, the ultimate loads at one, seven, and 28 days were 3.42 kN (0.77 kips), 6.44 kN (1.45 kips), and 6.74 kN (1.52 kips), respectively. This observation indicates that the surface energy controlling the adhesion between the bonding agent and CFRP reached its almost maximum after seven days of curing. The interfacial strength of the cement mortar at early ages (less than one day) was attributed to van der Waals forces (Liu et al. 2014) until the chemical bond took over the primary adhesion (Berenguer et al. 2021). The average capacity of the specimens with the polyester-silica resin consistently developed up to 14 days and then the response slope became less stiff [Figure I5(b)]. The above-stated chain reactions of polyester generated the strength and adhesion of the composite resin and, as the entangled chains successively formed, the development rate of the bond against CFRP decelerated. The temporal pattern of specimens with UHPC [Figure I5(c)] was distinct from those of the previous cases. The 28-day ultimate loads of the UHPC-bonded prisms were comparable with the loads of the polyester-silica prisms: 22.49 kN (5.06 kips) vs. 23.52 kN (5.29 kips), on average. Given that the adhesion of UHPC was virtually constant after three days, this type of resin is recommendable for time-sensitive applications such as an emergency strengthening project. The capacity variation of the specimens with geopolymer [Figure I5(d)] was analogous to their mortar counterparts [Figure I5(a)]. It should be pointed out that the compression and adhesion strengths of these resins were not proportional. The 28-day average compression strength of the geopolymer and mortar was 24.4 MPa (3,539 psi) and 12.5 MPa (1,813 psi), respectively, while the 28-day interfacial capacities were 5.25 kN (1.18 kips) and 6.74 kN (1.52 kips), respectively, on average. Further discussions on the cohesion and adhesion of inorganic resins are available elsewhere (Maso 1992).

Cluster analysis—Figures I6(a) to (c) demonstrate the clustering of the interfacial capacities, based on a mathematical processing technique called K-means, which can partition the boundaries of the resins' performance and identify their similarities. The concept of the K-means clustering is that the centroids of given data are set and iteratively updated until the optimized groups are computed with minimal errors (Capo et al. 2020)

$$E(c) = \sum \left\| x - c_x \right\|^2 \tag{I2}$$

where $E(c)$ is the error function to be minimized, x is the data point, and c_x is a set of the centroids. Upon confirming the convergence of overall Euclidean distances between the capacities and corresponding centroids [Figure I6(a)], four clusters were identified [Figure I6(b)]. The individual clusters were then reassigned in time domain to characterize the attributes of the inorganic resins for NSM CFRP application [Figure I6(c)]. Within the 28-day investigation range, the performance of the mortar and geopolymer resins was similarly ranked at Clusters 1 and 2. The specimens with polyester-silica were classified into Cluster 3 between one and seven days, beyond which they were elevated to Cluster 4. Such a transition illustrates that the bilinear interfacial resistance of the polyester-silica-bonded CFRP [Figure I5(b)] was refined to be two segments before and after seven days of curing. The one-day capacities of the UHPC-bonded prisms were positioned in dual clusters, implying local uncertainty; nonetheless, the capacities were continually ranked at Cluster 4 after three days, which supports the reliable bond of the cured UHPC resin.

To elaborate on similarities between the clustered categories, statistical examinations were conducted using the two-sample t-test (Montgomery 2013)

$$t_0 = \frac{\bar{y}_1 - \bar{y}_2}{\sqrt{\frac{S_1^2}{n_1} + \frac{S_2^2}{n_2}}} \tag{I3}$$

$$v = \frac{\left(\frac{S_1^2}{n_1} + \frac{S_2^2}{n_2} \right)^2}{\frac{\left(S_1^2 / n_1 \right)^2}{n_1 - 1} + \frac{\left(S_2^2 / n_2 \right)^2}{n_2 - 1}} \tag{I4}$$

where t_0 is the test statistic; $\bar{y}_1$ and $\bar{y}_2$ are the means of the sample categories with sizes n_1 and n_2, respectively; S_1 and S_2 are the standard deviations; and v is the degrees of freedom. In line with the findings from the K-means clustering, the test statistics of the cases with mortar vs. geopolymer and polyester-silica vs. UHPC were calculated and are graphed in Figure I6(d). The critical values at a confidence interval of 95% were collected from the t distribution (Montgomery 2013) and connected to define a threshold line distinguishing the equality and inequality of the sample categories. The test statistics of the mortar-geopolymer couple were not stable from one to seven days, whereas the t_0 values were below the critical line after 14 days. It is inferred that the performance of these resins became equal after two weeks of curing from a statistical perspective. For the polyester-silica-UHPC couple, the test statistics plummeted after seven days and were maintained within the equality zone at an average of t_0 = 0.326 underneath the critical line, agreeing with the results of the cluster analysis.

4.4 Failure Mode

Figure I7 shows the failure mode of the CFRP-resin interface near the loaded end. The mortar resin cured for one day failed because of the insufficient adhesion against the concrete substrate [Figure I7(a), left]; however, at 28 days, the interfacial slip of the CFRP strip resulted in the failure of the specimen [Figure I7(a), right]. This fact signifies that the failure plane of the NSM CFRP system shifted from the concrete side to the strip side as the mortar curing progressed. On the polyester-silica resin, the pull-out of the strips was accompanied by the disintegration of the resin mixture [Figure I7(b)] irrespective of curing time. Contrary to other bonding agents possessing powder grains, the relatively large particles of the silica sand (nominal size = 0.45 mm [0.018 in.]) brought about stress concentrations at the contact surface with the hardened polyester matrix (Erofeev et al. 2020); accordingly, the agglomerated particles were in part separated from the composite resin. Regarding the UHPC, no damage was noticed in the resin when the strip was pulled and slipped along the interface [Figure I7(c)]. The geopolymer-bonded cases revealed interfacial slips [Figure I7(d)], while the local cohesion failure at one day reaffirms that the chemical bond of geopolymers with aluminosilicates develops during the first 30 hours of casting (Wang et al. 2021).

4.5 Load-Displacement

The load-displacement behavior of the interface test prisms is given in Figure I8 [selected cases are displayed for clarity and the repeated responses of the individual groups were alike, as shown in the inset of Figure I8(a)]. With the increased curing time, both strength and deformability were enhanced in the mortar-bonded specimens [Figure I8(a)]; nonetheless, the stiffness of the interface remained unchanged. Considering that the deformation of the mortar is dominated by the interfacial transition zone (ITZ) between the cement and sand (Liang et al. 2017), additional curing does not seem to influence the ITZ properties related to the invariant pre-peak stiffness. The interface bonded with polyester-silica demonstrated a steady growth in the load-displacement curve [Figure I8(b)]. Contingent upon the degree of curing, two kinds of post-peak responses were observed: softening and abrupt load drops. The progressively diminishing load resistance of the one-day-cured specimen means that the chemical reactions between the maleic anhydride and methyl ethyl ketone peroxide of the polyester composite were yet incomplete, so that a crosslinking process for the molecular structure was underway (Martin 2007). When the viscous liquid of the composite was fully converted to a solid state [7 and 28 days in Figure I8(b)], the failure became brittle. Figures I8(c) and (d) compare the overall behavior of the four inorganic resins at three and 28 days. Except for the specimen with UHPC, the initial slopes of those with other resins were akin to one another. The post-peak graphs belonging to the mortar and geopolymer resins exhibited marginal changes with time; by contrast, a dramatic improvement was seen for the polyester-silica resin owing to the foregoing reaction mechanism. As the strength of UHPC increased, the displacement of the CFRP interface at the peak load lessened. The literature describes that, according to scanning electron microscopy, the constituent structure of UHPC became dense with an increase in curing time (Hiremath and Yaragal 2017); consequently, the dislocation of the cement-bound grains in the UHPC mixture was restrained and the interfacial displacement was reduced. The stepwise load drops in the post-peak region of the prisms bonded with UHPC are ascribed to the sequential interlocking of the sliding strip along the groove, resulting from the kinetic friction between the contact surfaces of CFRP and UHPC.

4.6 Interfacial Energy

Figure I9 shows the specimens' interfacial energy, which was obtained from numerically integrating the area under the individual load-displacement curve until the peak load was reached [Figure I9(a), inset]. Albeit scattered, the energy of all cases went up with time [the application of mortar is provided in Figure 9(a)] and regression equations were fitted to represent the interfacial characteristics of the resins

$$E(t) = C_1 t^{C_2} \tag{I5}$$

where $E(t)$ is the predicted interfacial energy in kNmm; C_1 and C_2 are the empirical constants (Table I2); and t is the curing time in days. As charted in Figure I9(b), the predicted energy matched with the average experimental values. The development of the interfacial energy at a certain curing period is assessed in Figure I9(c) using Eq. I5, which was normalized by the energy at 28 days for comparison. The gradients of the mortar and polyester-silica cases were nearly linear, denoting that the interfacial resistance evenly increased over time. Contrarily, the geopolymer resin manifested a parabolic trajectory due to the precipitously rising energy for the first three days of curing. The normalized energy of the UHPC resin was plateaued and was insusceptible to the curing time. The energy growth rate of the geopolymer resin was higher than the rates of the mortar and polyester-silica resins at three days; then, an opposite trend was found after 14 days [Figure I9(d)]. On account of the quick energy accumulation, the rate was substantially lower for the interface with UHPC.

5. THEORETICAL ASSESSMENT

Analytical models are implemented to understand functional equivalence between organic and inorganic resins. By gauging the level of hazard, the failure risk of an NSM CFRP system is estimated.

5.1 Epoxy-Bonded Interface

Published experimental data were collected to represent the characteristics of an epoxy-bonded interface. Only CFRP strips similar to the one used in the current study were considered, and 107 samples were selected (Teng et al. 2006; Seracino et al. 2007; Oehlers et al. 2008; Rashid et al. 2008; Palmierri and Matthys 2010; Ceroni et al. 2012; Khshain et al. 2015; Peng et al. 2015; Zhang and Yu 2017). The fracture energy of the individual specimens (G_F) was then calculated (De Lorenzis and Teng 2007)

$$G_F = \frac{\sigma_{\max}^2 t_f}{2E_f} \tag{I6}$$

where σ_{max} is the maximum stress of NSM CFRP until failure; and t_f and E_f are the thickness and elastic modulus of CFRP, respectively. Figure I10(a) establishes a relationship between the maximum CFRP stress and the interfacial fracture energy. A linear tendency was noted between these variables, signifying that the increased CFRP stress provoked the deformation of the interface. As depicted in Figure I10(b), 80.4% of the specimens were positioned below a fracture energy value of 40 kJ/m^2 (2.8 kips-ft/ft^2) within the sampled boundaries of 123 GPa (17.8 ksi) $\leq E_f \leq$ 213 GPa (30.9 ksi) and 15 MPa (2,175 psi) $\leq f'_c \leq$ 60 MPa (8,702 psi). For modeling convenience, the discrete histogram of the fracture energy with the epoxy-bonded NSM CFRP interface was converted to

$$PDF\left(G_F\right)_{ep} = \frac{1}{0.73G_F}\phi\left(\frac{\ln\left(G_F - 3.22\right)}{0.73}\right) \tag{I7}$$

where PDF$(G_F)_{ep}$ is the probability density function and G_F is the fracture energy. The normality test based on the experimental data confirmed that the distribution was lognormal [Figure I10(c), inset].

5.2 Comparison between Organic and Inorganic Resins

The fitted interfacial energy of the specimens with the inorganic resins (Eq. I5) was divided by the bonded area to determine the respective fracture energy with time. Afterward, the probability of equivalence ($Pr(eq)$) was defined in Eq. I8 and inferred against the G_F of the organic resin within a temporal frame from $t = i$ to j

$$\Pr\left(eq\right) = \int_{t=i}^{t=j} PDF\left(G_F\right)_{ep} dG_F \tag{I8}$$

The physical significance of Eq. I8 is that it quantifies the functional equivalence between the organic and inorganic resins for the NSM CFRP system. Different from the mortar and geopolymer resins manifesting negligible conformance to the epoxy resin, the interface with the polyester-silica and UHPC resins showed an equivalence probability of up to 0.37 at 28 days [Figure I10(d)]. Even if the percentage appears low, the performance of these resins is expected to be as adequate as that of the epoxy because

their fracture energy is much higher than the typical value of 0.1 kJ/m^2 (0.007 kip-ft/ft^2) for concrete (*fib* 2001). In other words, NSM systems that strengthen a structural beam fail by the fracture of the concrete substrate before the CFRP-resin interface completely dissipates the internal energy, which accounts for the laboratory observations documented in many experimental programs (Haddad and Almomani 2017; Sharaky et al. 2018; Suliman et al. 2021).

5.3 Hazard Evaluation

The failure rate of the interface with the inorganic resins was investigated using a hazard function (Cornell 1967; Huang et al. 2018)

$$h(G_F) = \frac{f(G_F)}{1 - F(G_F)} \tag{I9}$$

$$f(G_F) = \frac{\alpha (G_F)^{\alpha-1}}{\beta^{\alpha}} \exp\left(-\left(\frac{G_F}{\beta} \right)^{\alpha} \right) \tag{I10}$$

$$F(G_F) = 1 - \exp\left(-\left(\frac{G_F}{\beta} \right)^{\alpha} \right) \tag{I11}$$

$$\alpha = COV_{G_F}^{-1.08} \tag{I12}$$

$$\beta = \frac{\mu_{G_F}}{\Gamma(1/\alpha + 1)} \tag{I13}$$

where $h(G_F)$ is the hazard function with the fracture energy (G_F) of the interface; α and β are the Weibull constants; μ_{G_F} and COV_{G_F} are the mean and coefficient of variation of G_F (the fitted fracture energy and the average COV of the test data were employed), respectively; and Γ is the gamma function. To solve the hazard function with the two-parameter Weibull distributions, the α and β constants were calculated [Figure I11(a)]. The hazard vs. fracture energy of the interface bonded with the polyester-silica resin is provided in Figure I11(b). As the curing of the resin progressed, the hazard level dwindled and the fracture energy increased. A conspicuous reduction of 60.9% in the maximum hazard was estimated between one and three days [Figure I11(b), inset], aligning with the incomplete chemical reactions during the early ages discussed above. Figure I11(c) shows the hazard levels of each resin at one day. The risk of failure, represented by a hazard value, was significantly high in the mortar and geopolymer resins, and the risk of the UHPC resin was the lowest. The time-dependent maximum hazard values of the resins are evaluated in Figure I11(d). The discrepancy between the one- and 28-day curing periods was largest in the polyester-silica resin (90.4%), followed by the mortar and geopolymer resins (66.7% and 56.9%, respectively). The risk of using the UHPC resin was consistently low.

6. SUMMARY AND CONCLUSIONS

The first part of this report has studied the time-dependent behavior of NSM CFRP strips interfaced with inorganic resins: mortar, polyester-silica, UHPC, and geopolymer. The suitability of these resins was examined for NSM application via rheological characteristics and mechanical performance from casting to 28 days. In order to theoretically clarify the vector quantization and failure rate of the CFRP-inorganic resin interface, statistical analysis was conducted, and analytical models were formulated. The functional equivalence of the inorganic resins against conventional organic bonding agents was quantified as well. The following conclusions are drawn.

- The rheological resistance of the polyester-silica and UHPC resins increased after 20 to 30 minutes of casting due to the progression of a setting process; on the other hand, such resistance was not noticed in the mortar and geopolymer resins up to 60 minutes. The strain rate of the polyester resin was more reactive to viscosity in comparison with others.
- The hydration of mortar became apparent after one day of casting and continued over 28 days, involving hydrated calcium silicates, crystallized calcium hydroxide, and reduced free water in the capillaries. There was an analogy between the mortar and geopolymer in terms of strength gain. On average, the compressive strength of polyester-silica steadily developed to 35 MPa (5,076 psi) at 28 days in tandem with condensation reactions, molecular gelation, and vitrification. The early-age strength of UHPC was noteworthy (61.9 MPa [8,978 psi] and 95.3 MPa [13,822 psi] at one and three days, respectively), and the 28-day strength was 120 MPa (17,000 psi).
- Regarding the time-dependent response of the CFRP-resin interface, the capacities of the specimens bonded with mortar and geopolymer went up to seven days and leveled out; in contrast, the interfacial capacity of polyester-silica continued to rise until 28 days in a bilinear manner. The adhesion of the CFRP-UHPC interface became constant after three days and stabilized. The capacities of the interface with the mortar and geopolymer and the polyester-silica and UHPC resins were clustered, and their statistical similarities were classified at a confidence interval of 95%.
- The failure plane of the mortar-bonded interface relocated from the resin-concrete to the resin-CFRP regions over time. The failure of all other specimens was attributed to the interfacial slip of CFRP, regardless of curing period. Although the strength and deformability of the mortar interface were enhanced with the increased curing process, marginal changes were noticed in the stiffness. The post-peak response of the specimens bonded with polyester-silica varied by curing time: smooth vs. precipitous load drops at one day and after seven days, respectively. The failure mode of the UHPC-bonded interface was abrupt, while that of the geopolymer-bonded interface was gradual. Unlike other resin types, the growth of interfacial energy in the specimens with UHPC was virtually time-invariant.
- As per the probability-based calculation of functional equivalence, the performance of the interface with polyester-silica and UHPC was comparable to the case of organic epoxies. The level of hazard, representing the risk of failure, was evidently high in the mortar- and geopolymer-bonded interface.

7. REFERENCES

ACI. 2007. *Report on Fiber-Reinforced Polymer (FRP) Reinforcement for Concrete Structures* (ACI 440R-07), American Concrete Institute Committee 440, Farmington Hills, MI.

ACI. 2017. *Guide for the Design and Construction of Externally Bonded FRP Systems for Strengthening Concrete Structures* (ACI 440.2R-17), American Concrete Institute Committee 440, Farmington Hills, MI.

ACI. 2018. *Ultra-High Performance Concrete: An Emerging Technology Report* (ACI 239R-18), American Concrete Institute Committee 239, Farmington Hills, MI.

Ahmad, M.R., and Chen, B. 2020. "Microstructural characterization of basalt fiber reinforced magnesium phosphate cement supplemented by silica fume," *Construction and Building Materials*, 237, 117795.

Al-Jaberi, Z., Myers, J.J., and Chandrashekhara, K. 2019. "Effect of direct service temperature exposure on the bond behavior between advanced composites and CMU using NSM and EB techniques," *Composite Structures*, 211, 63-75.

Al-Saadi, N.T.K., Mohammed, A., Al-Mahaidi, R., and Sanjayan, J. 2019. "A state-of-the-art review: Near-surface mounted FRP composites for reinforced concrete structures," *Construction and Building Materials*, 209, 748-769.

Arnoult, M., Perronnet, M., Autef, A., and Rossignol, S. 2019. "Geopolymer synthetized using reactive or unreactive aluminosilicate understanding of reactive mixture," *Materials Chemistry and Physics*, 237, 121837.

ASTM. 2010. "Standard test method for determining the penetration of chloride ion into concrete by ponding" (ASTM C1543), American Society for Testing and Materials, West Conshohocken, PA.

ASTM. 2015a. "Standard test method for resistance of concrete to rapid freezing and thawing" (ASTM C666), American Society for Testing and Materials, West Conshohocken, PA.

ASTM. 2015b. "Standard test method for measuring changes in height of cylindrical specimens of hydraulic-cement grout" (ASTM C1090), American Society for Testing and Materials, West Conshohocken, PA.

ASTM. 2018. "Standard test method for compressive strength of cylindrical concrete specimens" (ASTM C39), American Society for Testing and Materials, West Conshohocken, PA.

ASTM. 2020a. "Standard test method for time of setting of hydraulic cement mortar by modified vicat needle" (ASTM C807), American Society for Testing and Materials, West Conshohocken, PA.

ASTM. 2020b. "Standard test method for compressive strength of hydraulic cement mortars (using 2-in. or [50 mm] cube specimens)" (ASTM C109), American Society for Testing and Materials, West Conshohocken, PA.

ASTM. 2021. "Standard specification for flow table for use in tests of hydraulic cement" (ASTM C230), American Society for Testing and Materials, West Conshohocken, PA.

Barnes, H.A., Hutton, J.F., and Walters, K, *An introduction to rheology*, Elsevier, Amsterdam, The Netherlands.

Bauer, E., de Sousam J.G.G., Guimaraes, E.A., and Silva, F.G.S. 2007. "Study of the laboratory Vane test on mortars," *Building and Environment*, 42, 86-92.

Berenguer, R.A., Lima, N.B., Lima, V.M.E., Estolano, A.M.L., Povoas, Y.V., and Lima, N.B.D. 2021. "The role of hydrogen bonds on the mechanical properties of cement-based mortars applied to concrete surfaces," *Cement and Concrete Composites*, 115, 103848.

Capo, M., Perez, A., and Lozano, J.A. 2020. "An efficient K-means clustering algorithm for tall data," *Data Mining and Knowledge Discovery*, 34, 776-811.

CDOT. 2018. "Revision of section 601: ultra high performance concrete," Colorado Department of Transportation, Denver, CO.

Ceroni, F., Pecce, M., Bilotta, A., and Nigro, E. 2012. "Bond behavior of FRP NSM systems in concrete elements," *Composites Part B*, 43(2), 99-109.

Chokrieh, M.M., Rezvani, S., and Mosalmani, R. 2015. "A novel polymer concrete made from fine silica sand and polyester," *Mechanics of Composite Materials*, 51(5), 571-580.

Cornell, C.A. 1967. "Bounds on the reliability of structural systems," *Journal of Structural Division*, 93(1), 171-200.

Costa, E.B.C., Cardoso, F.A., and John, V.M. 2017. "Influence of high contents of limestone fines on rheological behaviour and bond strength of cement-based mortars," *Construction and Building Materials*, 156, 1114-1126.

De Lorenzis, L., and Teng, J.G. 2007. "Near-surface mounted FRP reinforcement: an emerging technique for strengthening structures," *Composites Part B*, 38, 119-143.

Erofeev, V., Fomin, N., Ivlev, V., Yudin, V., and Myshkim, A. 2020. "Cyclic strength of polyester acrylate composites," IOP Conference Series: Materials Science and Engineering, 896, 012110.

Evans, S.J., Haines, P.J., and Skinner, G.A. 1996. "The effects of structure on the thermal degradation of polyester resins," *Thermochimica Acta*, 278, 77-89.

Feng, S., Xiao, H., and Li, H. 2020. "Comparative studies of the effect of ultrahigh-performance concrete and normal concrete as repair materials on interfacial bond properties and microstructure," *Engineering Structures*, 222, 111122.

fib. 2001. "Externally bonded FRP reinforcement for RC structures (Bulletin 14)," Task Group 9.3, Federation Internationale du Beton, Lausanne, Switzerland

Haddad, R.H., and Almomani, Q.A. 2017. "Recovering flexural performance of thermally damaged concrete beams using NSM CFRP strips," *Construction and Building Materials*, 154, 632-643.

Hashemi, S., and Al-Mahaidi, R. 2012. "Experimental and finite element analysis of flexural behavior of FRP-strengthened RC beams using cement-based adhesives," *Construction and Building Materials*, 26, 268-273.

Hiremath, P.N., and Yaragal, S.C. 2017. “Effect of different curing regimes and durations on early strength development of reactive powder concrete,” *Construction and Building Materials*, 154, 72-87.

Hlavacek, P., Sulc, R., Smilauer, V., Robler, C., and Snop, R. 2018. “Ternary binder made of CFBC fly ash, conventional fly ash, and calcium hydroxide: phase and strength evolution,” *Cement and Concrete Composites*, 90, 100-107.

Huang, B.-T., Li, Q.-H., Xu, S.-L., Liu, W., and Wang, H.-T. 2018. “Fatigue deformation behavior and fiber failure mechanism of ultra-high toughness cementitious composites in compression,” *Materials and Design*, 157, 457-468.

Graybeal, B. 2014. “Design and construction of field-cast UHPC connections,” Tech Note FHWA-HRT-14-084, Federal Highway Administration, Washington, D.C.

Jankovic, B. 2010. “The kinetic analysis of isothermal curing reaction of an unsaturated polyester resin: Estimation of the density distribution function of the apparent activation energy,” *Chemical Engineering Journal*, 162, 331-340.

Jonsson, B., Nonat, J.A., Labbez, C., Cabane, B., and Wennerstrom, H. 2005. “Controlling the cohesion of cement paste,” *Langmuir*, 21(20), 9211-9221.

Khshain, N.T., Al-Mahaidi, R., and Abdouka, K. 2015. “Bond behaviour between NSM CFRP strips and concrete substrate using single-lap shear testing with epoxy adhesive,” *Composite Structures*, 132, 205-214.

Li, Z., Ding, Z., and Zhang, Y. 2004. “Development of sustainable cementitious materials,” Proceedings of the International Workshop on Sustainable Development and Concrete Technology, 55-76.

Liang, S., Wei, Y., and Wu, Z. 2017. “Multiscale modeling elastic properties of cement-based materials considering imperfect interface effect,” *Construction and Building Materials*, 154, 567-579.

Liu, Y., Wang, F., Liu, M., and Hu, S. 2014. “A microstructural approach to adherence mechanism of cement and asphalt mortar (CA mortar) to repair materials,” *Construction and Building Materials*, 66, 125-131.

Mandredi, L.B., Rodriguez, E.S., Wladyka-Przybylak, M., and Vazquez, A. 2006. “Thermal degradation and fire resistance of unsaturated polyester, modified acrylic resins and their composites with natural fibres,” *Polymer Degradation and Stability*, 91, 255-261.

Martin, J.L. 2007. “Kinetic analysis of two DSC peaks in the curing of an unsaturated polyester resin catalyzed with methylethylketone peroxide and cobalt octoate,” *Polymer Engineering and Science*, 47(1), 62-70.

Maso, J.C. 1992. *Interfaces in Cementitious Composites*, CRC Press, Taylor & Francis, Boca Raton, FL.

Montgomery, D.C. 2013. *Design and Analysis of Experiments* (8th edition), Wiley, Hoboken, NJ.

Neville, A.M. 1995. *Properties of Concrete: 4th edition*, Prentice Hall, Essex, UK

Oehlers, D.J., Haskett, M., Wu, C., and Seracino, R. 2008. “Embedding NSM FRP plates for improved IC debonding resistance,” *Journal of Composites for Construction*, 12(6), 635-642.

Palmierri, A., and Matthys, S. 2010. “Experimental investigation on bond of NSM strengthened RC structures,” 5th International Conference on FRP composites in Civil Engineering, 572-575.

Peng, H., Hao, H., Zhang, J., Liu, Y., and Cai, C.S. 2015. “Experimental investigation of the bond behavior of the interface between near-surface-mounted CFRP strips and concrete,” *Construction and Building Materials*, 96, 11-19.

Ramsey, M.S. 2019. “Rheology, viscosity, and fluid types,” *Practical Wellbore Hydraulics and Hole Cleaning*, 217-237.

Rashid, R., Oehlers, D.J., Seracino, R. 2008. “IC debonding of FRP NSM and EB retrofitted concrete: plate and cover interaction tests,” *Journal of Composites for Construction*, 12(2), 160-167.

Seracino, R., Jones, N.M., Ali, M.S.M., Page, M.W., and Oehlers, D.J. 2007. “Bond strength of near-surface mounted FRP strip-to-concrete joints,” *Journal of Composites for Construction*, 11(4), 401-409.

Sharaky, I.A., Baena, M., Barris, C., Sallam, H.E.M., and Torres, L. 2018. “Effect of axial stiffness of NSM FRP reinforcement and concrete cover confinement on flexural behaviour of strengthened RC beams: Experimental and numerical study,” *Engineering Structures*, 173, 987-1001.

Shi, Y., Long, G., Zen, X., Xie, Y., and Shang, T. 2021. “Design of binder system of eco-efficient UHPC based on physical packing and chemical effect optimization,” *Construction and Building Materials*, 274, 121382.

Snijkers, F., Pasquino, R., Olmsted, P.D., and Vlassopoulos, D. 2015. “Perspectives on the viscoelasticity and flow behavior of entangled linear and branched polymers,” *Journal of Physics: Condensed Matter*, 27, 473002.

Suliman, A.K.S., Jia, Y., and Mohammed, A.A.A. 2021. “Experimental evaluation of factors affecting the behaviour of reinforced concrete beams strengthened by NSM CFRP strips,” *Structures*, 32, 632-640.

Tailby, J., and MacKenzie, K.J.D. 2010. “Structure and mechanical properties of aluminosilicate geopolymer composites with Portland cement and its constituent minerals,” *Cement and Concrete Research*, 40, 787-794.

Taljsten, B., and Blanksvard, T. 2007. “Mineral-based bonding of carbon FRP to strengthen concrete structures,” *Journal of Composites for Construction*, 11(2), 120-128.

Tang, Y., Su, H., Huang, S., Qu, C., and yang, J. 2017. “Effect of curing temperature on the durability of concrete under highly geothermal environment,” *Advances in Materials Science and Engineering*, 2017, 7587853.

Teng, J.G., De Lorenzis, L., Wang, B., Li, R., Wong, T.N., and Lam, L. 2006. “Debonding failures of RC beams strengthened with near surface mounted CFRP strips,” *Journal of Composites for Construction*, 10(2), 92-105.

Vargas, M.A., Sachsenheimer, K., and Guthausen, G. 2012. “In-situ investigations of the curing of a polyester resin,” *Polymer Testing*, 31, 127-135.

Vasconcelos, E., Fernandes, S., de Aguiar, J.L.B., and Pacheco-Torgal, F. 2011. “Concrete retrofitting using metakaolin geopolymer mortars and CFRP,” *Construction and Building Materials*, 25, 3213-3221.

Wang, Y.-S., Peng, K.-D., Alrefaei, Y., and Dai, J.G. 2021. “The bond between geopolymer repair mortars and OPC concrete substrate: strength and microscopic interactions,” *Cement and Concrete Composites*, 119, 103991.

Wasim, M., Ngo, T.D., and Law, D. 2021. “A state-of-the-art review on the durability of geopolymer concrete for sustainable structures and infrastructure,” *Construction and Building Materials*, 291, 123381.

Xu, H., and Van Deventer, J.S.J. 2000. “The geopolymerisation of alumino-silicate minerals,” *International Journal of Mineral Processing*, 59, 247-266.

Yim, H.J., Lee, H., and Kim, J.H. 2017. “Evaluation of mortar setting time by using electrical resistivity measurements,” *Construction and Building Materials*, 146, 679-686.

Yu, J.-G., Cheng, L., Liu, S., Fu, B., and Li, B. 2021. “Inorganic adhesive based near-surface-mounted fibre reinforced polymer for strengthening of concrete structures: an overview,” *Structures*, 33, 2099-2120.

Zhang, S.S., and Yu, T. 2017. “Effect of groove spacing on bond strength of near-surface mounted (NSM) bonded joints with multiple FRP strips,” *Construction and Building Materials*, 155, 103-113.

Table I1. Interface test specimens [1 kN = 0.225 kips]

Time (days)	Interfacial capacity (kN)							
	Mortar		Polyester-silica		UHPC		Geopolymer	
	Each	Average	Each	Average	Each	Average	Each	Average
1	3.55	3.42	10.03	10.07	18.93	18.25	2.78	3.18
	3.46		10.84		19.61		3.38	
	3.24		9.33		16.22		3.38	
3	4.54	5.00	13.13	11.56	20.75	20.67	3.69	3.36
	5.12		11.64		22.63		3.65	
	5.34		9.90		18.64		2.73	
7	5.86	6.44	14.72	14.66	18.73	20.49	4.55	4.37
	6.77		15.53		21.00		4.18	
	6.68		13.72		21.75		4.38	
14	6.34	5.94	22.57	20.39	23.45	20.80	4.65	5.19
	6.14		18.26		18.20		4.67	
	5.34		20.35		20.75		6.26	
28	7.94	6.74	19.66	23.52	24.51	22.49	5.04	5.25
	6.08		25.05		22.85		5.73	
	6.20		25.85		20.10		4.98	

P_u = ultimate load

Table II2. Regression terms for interfacial energy

	Mortar	Polyester-silica	UHPC	Geopolymer
C_1	0.704	9.995	92.678	0.912
C_2	0.589	0.757	0.005	0.284

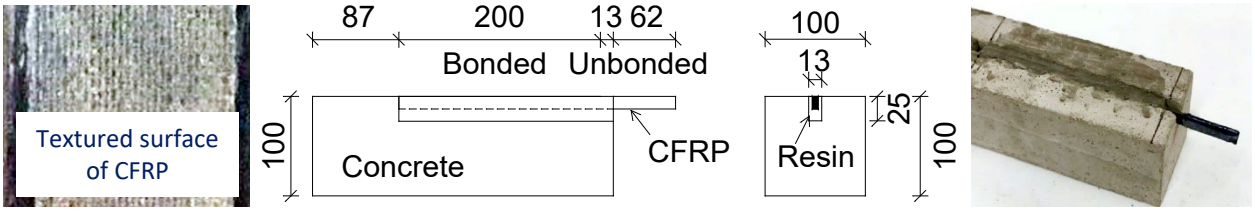

(a)

(b) (c) (d) (e)

Figure I1. Specimen details: (a) schematic of interface test specimen (units in mm [1 mm = 0.0394 in.]); (b) concrete cylinder; (c) inorganic resin cube; (d) rheology; (e) interface test

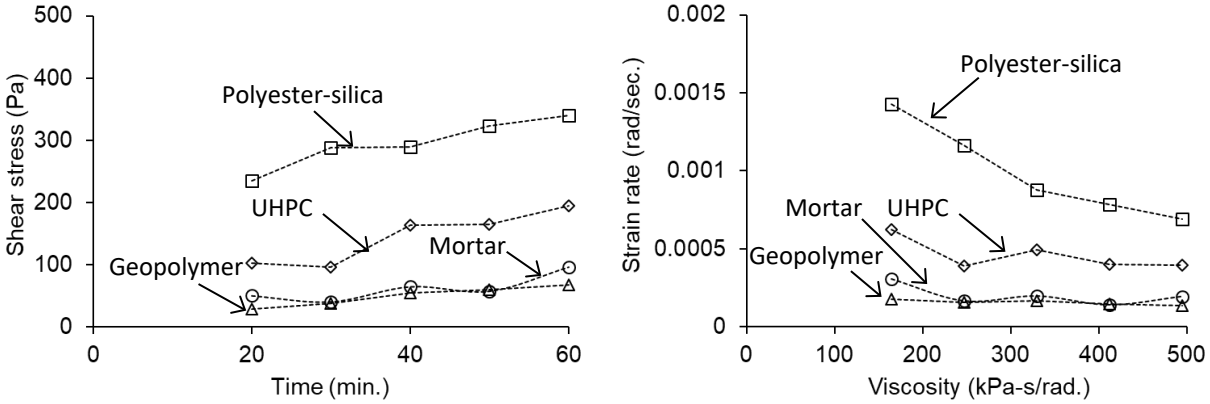

(a) (b)

[1 Pa = 0.021 psf; 1 kPa-s/rad. = 0.145 psi-s/rad.]

Figure I2. Early-age rheology of bonding agents: (a) shear stress; (b) strain rate

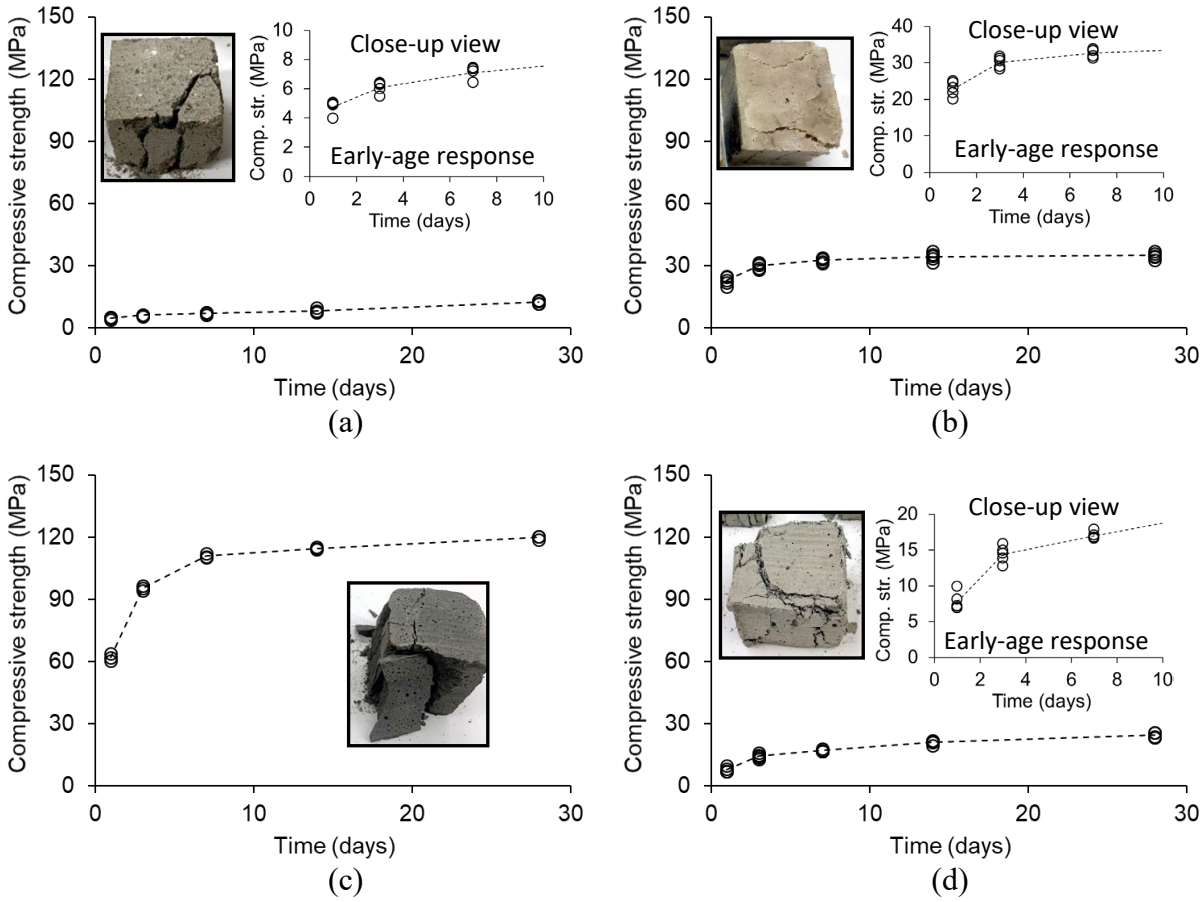

Figure I3. Compressive strength of inorganic resins: (a) mortar; (b) polyester-silica; (c) UHPC; (d) geopolymer

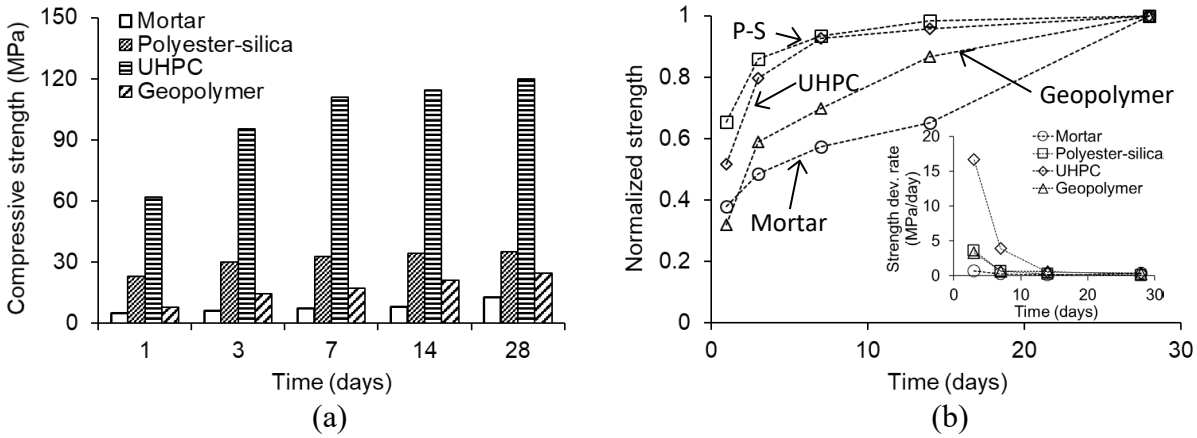

Figure I4. Characteristics of inorganic resins: (a) average strength; (b) strength development

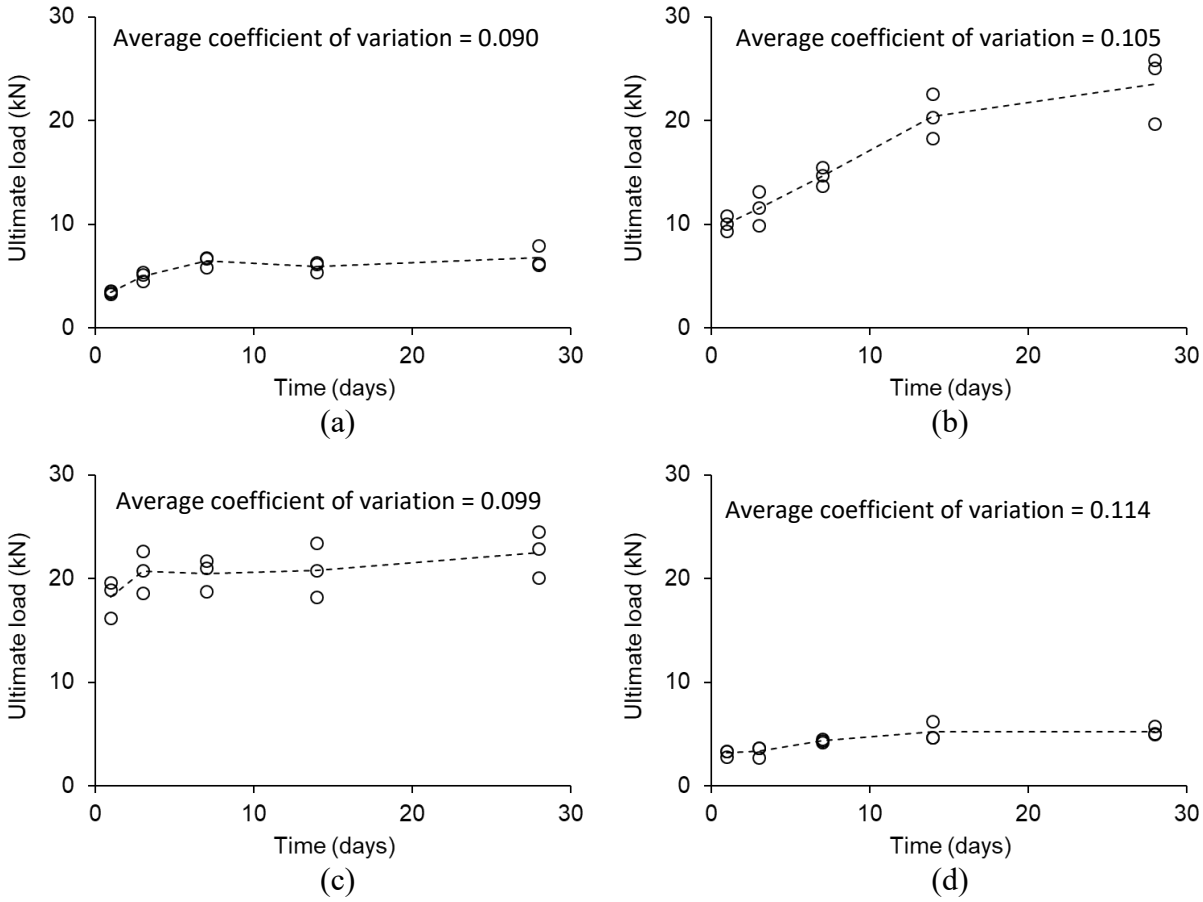

Figure I5. Interfacial capacity (dotted line = average): (a) mortar; (b) polyester-silica; (c) UHPC; (d) geopolymer

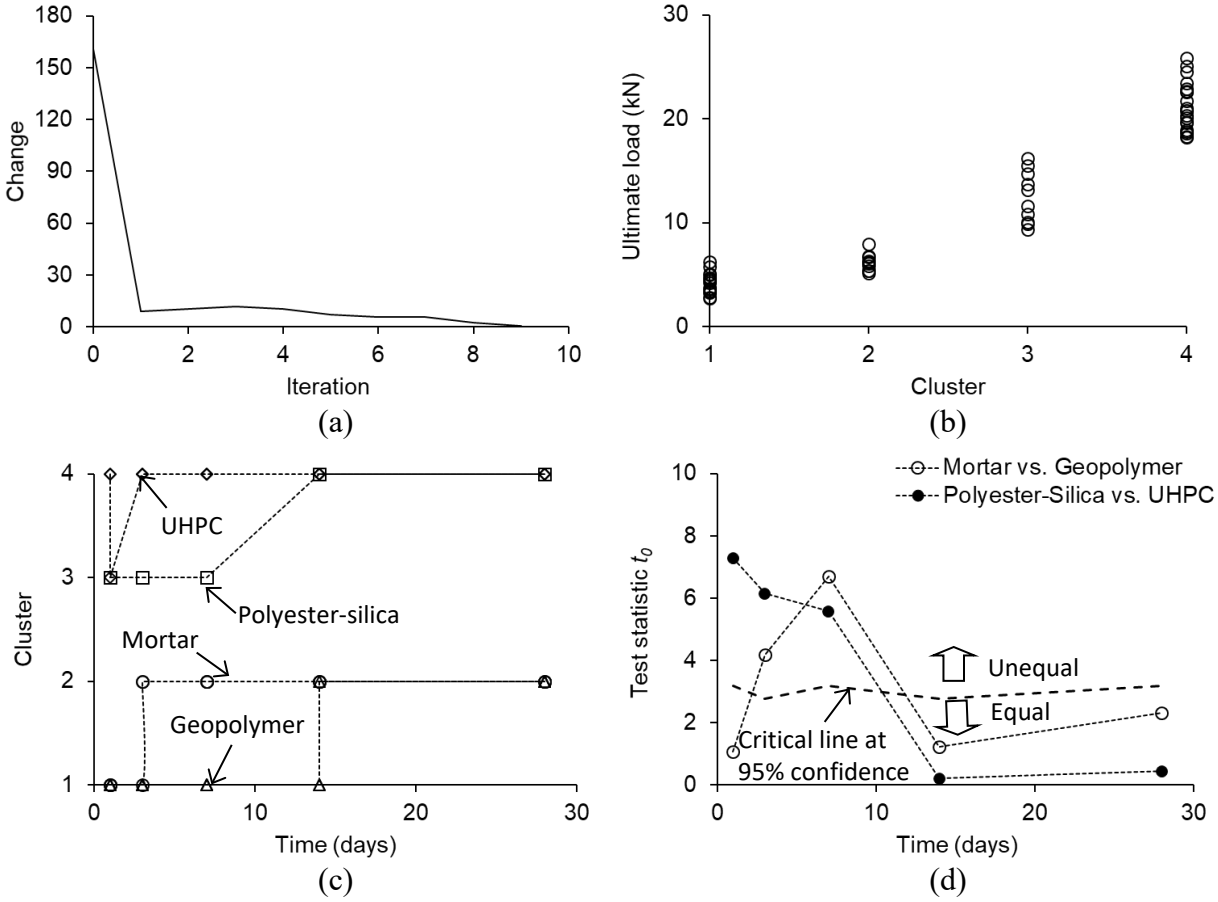

Figure I6. Cluster analysis: (a) convergence of centroids; (b) identified clusters; (c) variation of clusters; (d) t-test results

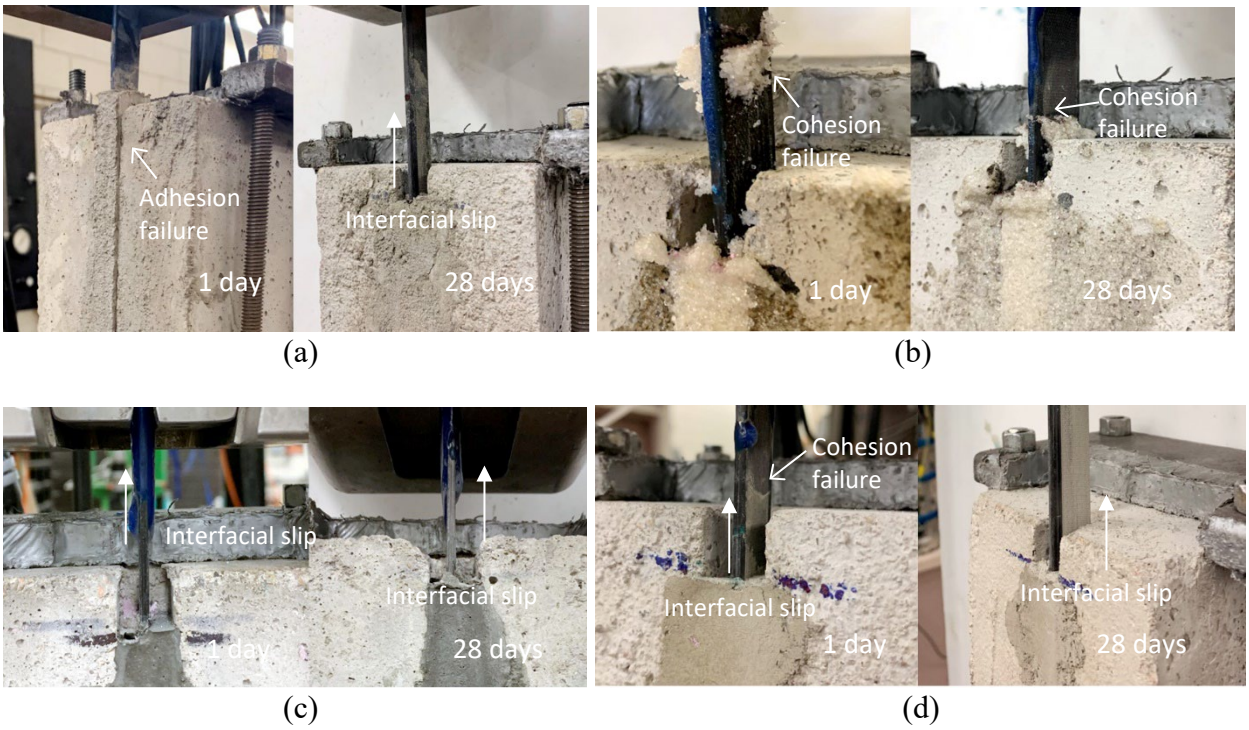

Figure I7. Failure mode: (a) mortar; (b) polyester-silica; (c) UHPC; (d) geopolymer

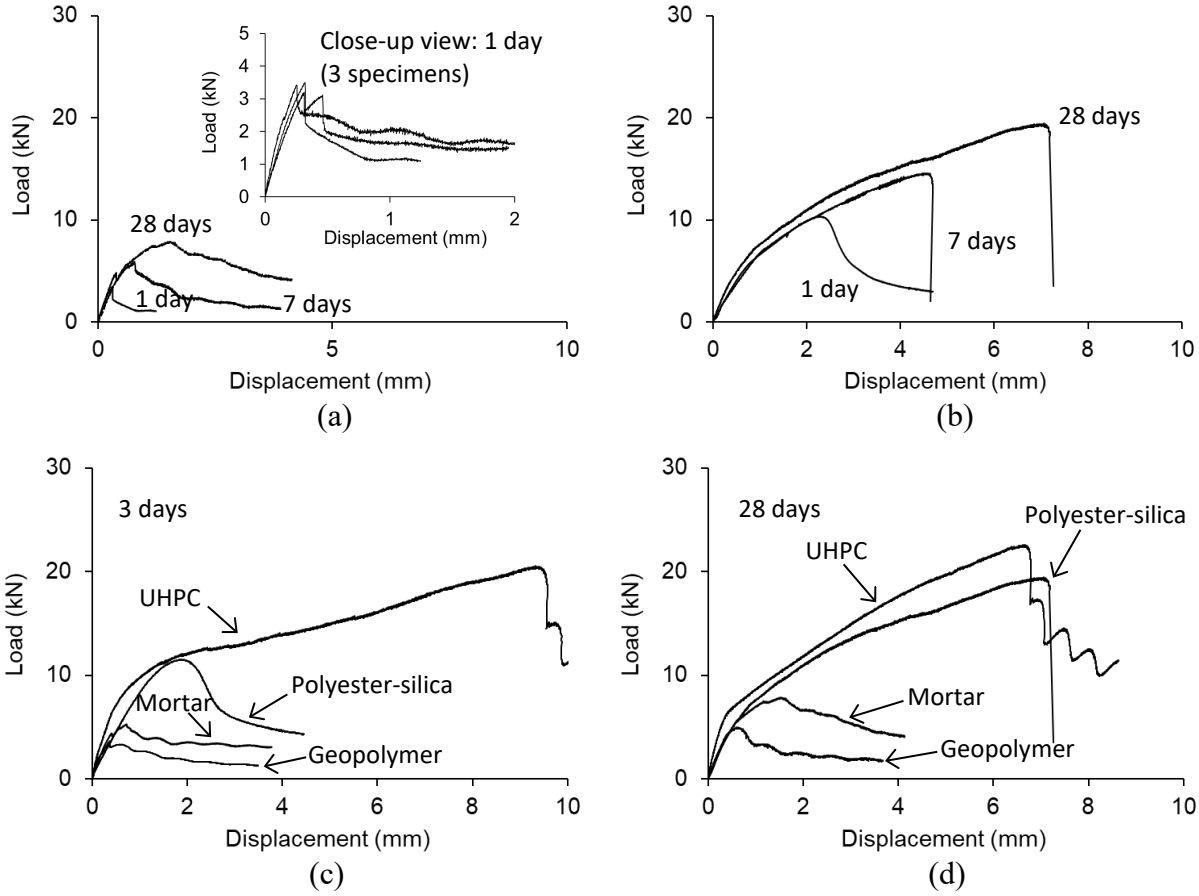

[1 kN = 0.225 kips; 1 mm = 0.0394 in.]

Figure I8. Load-displacement of interface specimens: (a) mortar; (b) polyester-silica; (c) comparison at 3 days; (d) comparison at 28 days

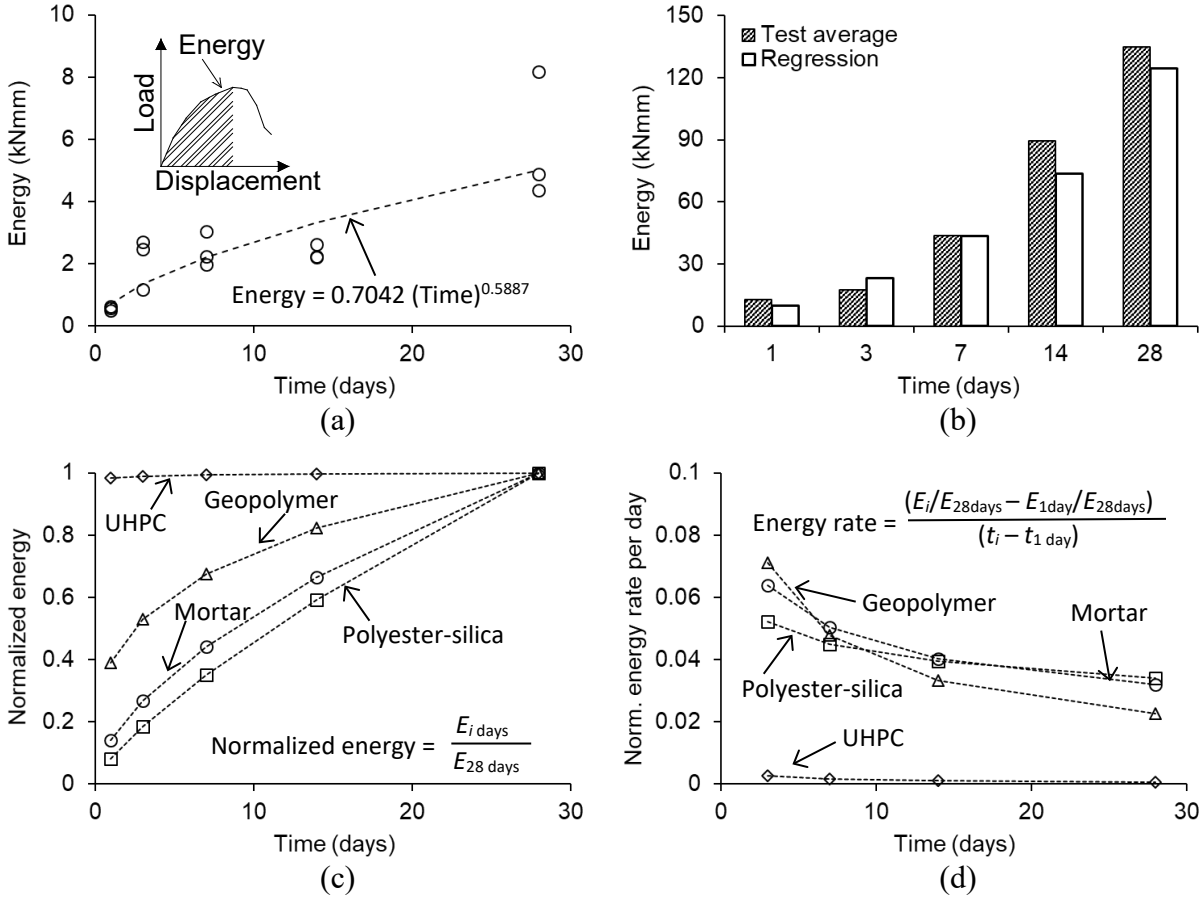

[1 kNmm = 8.87 lb-in.]

Figure I9. Interfacial energy: (a) mortar; (b) polyester-silica; (c) development over time; (d) development rate

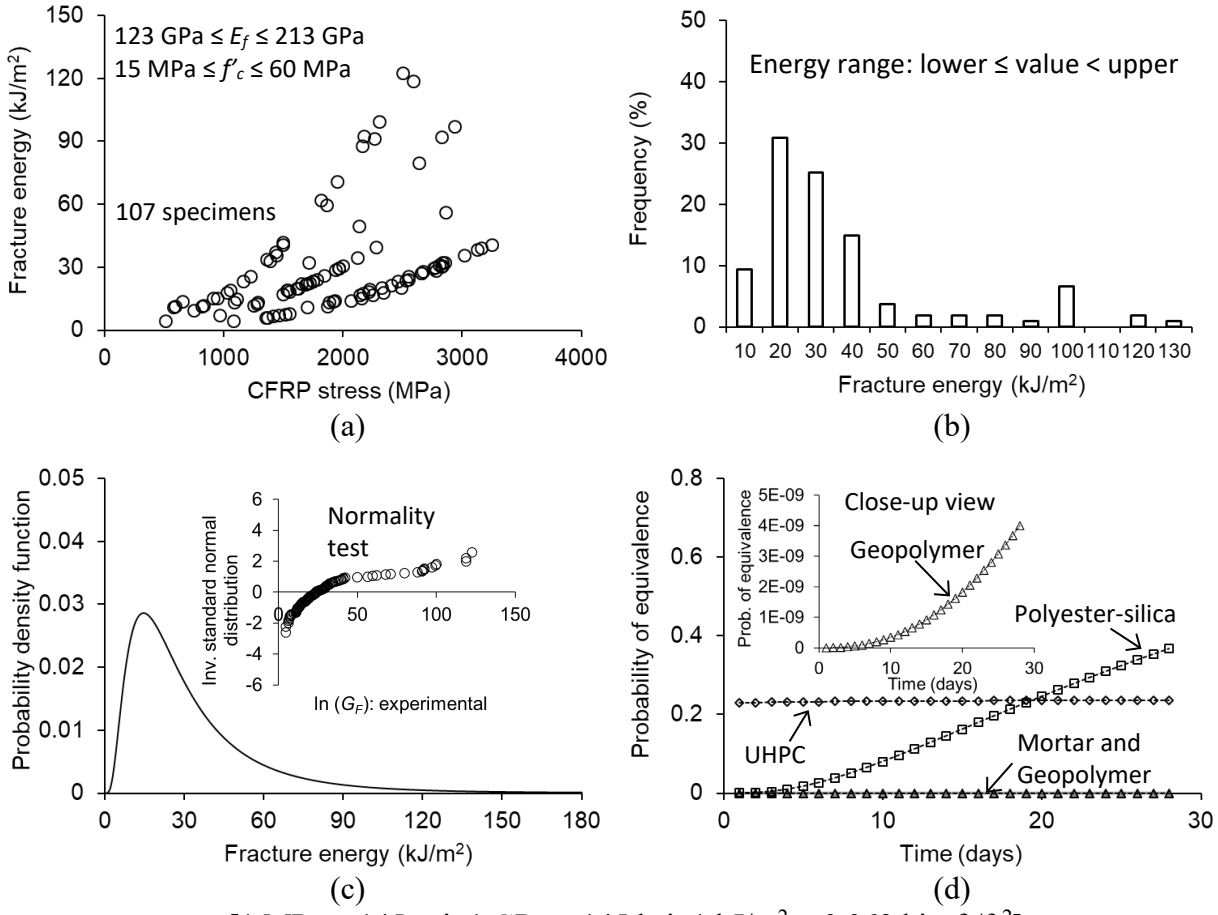

[1 MPa = 145 psi; 1 GPa = 145 ksi; 1 kJ/m^2 = 0.069 kip-ft/ft^2]

Figure I10. Assessment of equivalency against epoxy adhesive: (a) fracture energy vs. CFRP stress of epoxy-bonded interface; (b) frequency distribution of epoxy-bonded interface; (c) probability distribution; (d) equivalence probability between organic and inorganic resins for NSM CFRP

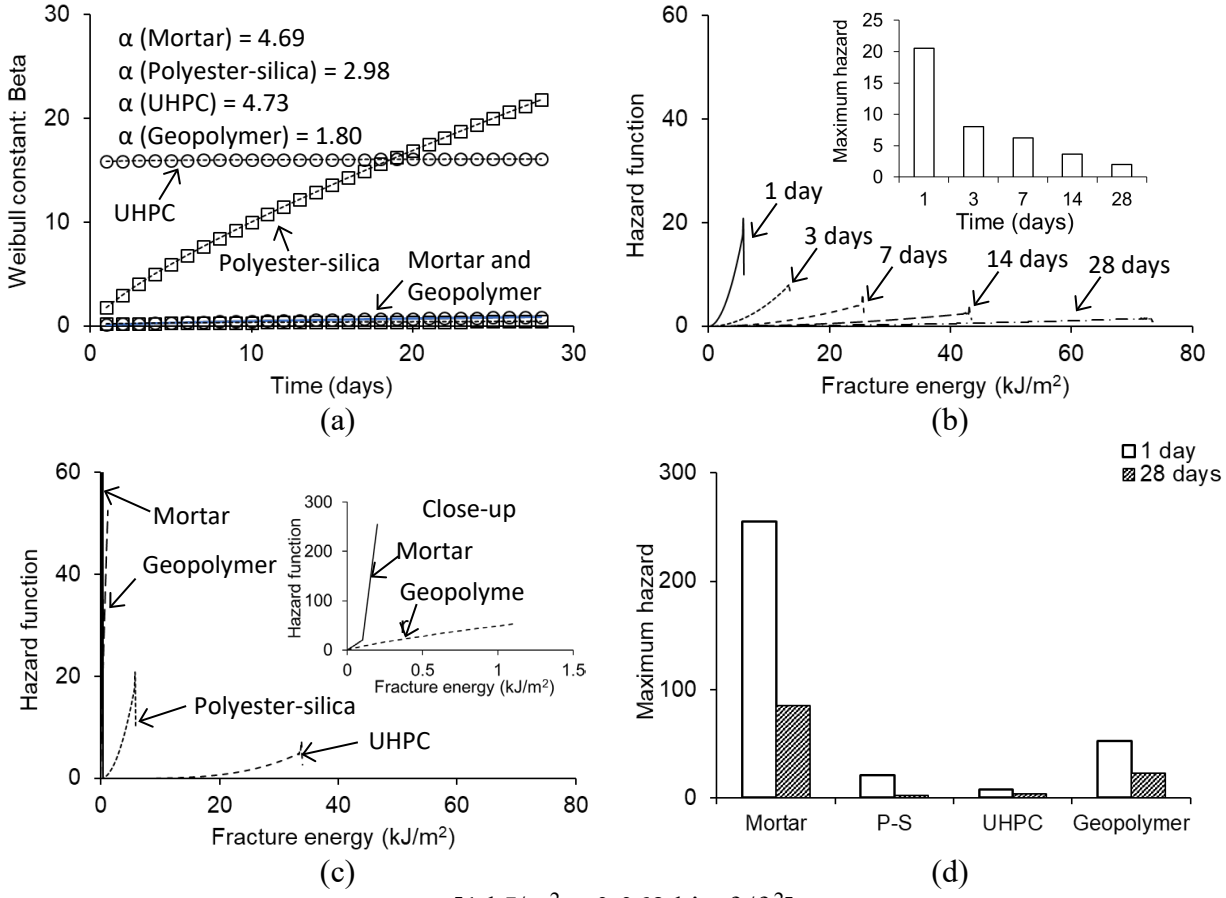

[1 kJ/m^2 = 0.069 kip-ft/ft^2]

Figure I11. Hazard evaluation: (a) constants; (b) hazard function of interface with polyester-silica; (c) hazard function at 1 day; (d) comparison among resins

Part II: Cementitious Resins for Strengthening RC Beams with NSM CFRP

8. INTRODUCTION

Socioeconomic demands are growing for the development of efficient and durable structural members to accomplish sustainable built-environments. Multidirectional endeavors, founded upon collaborative synergies between technical and public sectors, can relieve risk and vulnerability against man-made and natural hazards (Reddy 2022). In comparison with demolition and reconstruction, rehabilitation is deemed to be a competitive option that satisfies the stringent requirements of modern building codes at affordable expense (Aprile and Monti 2022). Accordingly, a number of retrofit methodologies have been proposed and executed using concrete jackets (Zaiter and Lau 2021), steel plates (Chung and Chou 2022), prestressing strands (Xue et al. 2020), bracings (Labo et al. 2020), energy-dissipating dampers (Zhang et al. 2021), and external frames (Cao et al. 2022). Among others, carbon fiber reinforced polymer (CFRP) composites have become a notable alternative for structural rehabilitation on account of many benefits: light weight, high strength and modulus, noncorrosiveness, tailorability, convenient installation, low maintenance, and longevity (ACI 2017). Prevalent CFRP-strengthening techniques are categorized into two groups: i) the EB method that CFRP sheets are externally bonded with a polymeric adhesive, and ii) the NSM method that CFRP strips are inserted into a precut groove and near-surface-mounted with a resin matrix. From an interfacial mechanics perspective, the NSM method is distinct from the EB method in that an integrated system is established between the adhesive and CFRP, which is beneficial in terms of transferring shear stress with the enlarged contact dimensions (Grande and Milani 2021). Retrofitting concrete members with NSM CFRP encompasses several advantages over EB CFRP, such as reduced labor, minimal surface preparation, debonding resistance, durability, and aesthetics (De Lorenzis and Teng 2007). The two main factors to be considered when choosing an appropriate bonding agent for installing NSM CFRP strips are strength and workability, because premature interfacial failure would lead to the malfunctioning of the strips and improper rheology could give rise to unnecessary impediments to the planned rehabilitation process.

The majority of research projects concerning NSM CFRP have been conducted with organic epoxies; consequently, contemporary design guidelines and specifications do not contain information on other substitutes (ACI 2010; ACI 2017). The need for inorganic resins arises, per contra, when a structure to be strengthened with CFRP is exposed to aggressive environments, which can readily degrade the bond of organic resins. Yang et al. (2015) reported the bond of NSM CFRP with an engineered cementitious composite consisting of cement, fly ash, silica fume, sand, a high-range water reducer, and polyvinyl alcohol fibers. The interfacial failure of CFRP with the cementitious resin was not as brittle as the failure with an epoxy resin. Al-Saadi et al. (2017) assessed the residual capacity of fatigue-damaged concrete beams strengthened with NSM CFRP incorporating a cementitious adhesive. Until failure occurred, debonding of CFRP was not observed and the interface transition zone between the strengthening system and the concrete seemed to be uniform. Kuntal et al. (2020) carried out a test program on the pull-out and shear-strengthening of concrete members with NSM CFRP. The bonding agent was a cement grout possessing a seven-day compressive strength of 45 MPa (6,526 psi). The installed CFRP strips inhibited the opening of cracks and lowered the evolution of concrete strains. Further details about NSM CFRP coupled with inorganic resins are covered in review articles (Elsanadedy et al. 2019; Yu et al. 2021).

Despite their rapid growth and auspicious potential, there is a dearth of knowledge on the application of cementitious resins for adhering NSM CFRP. Especially, the types of usable inorganic resins are still restrictive and, in most cases, ordinary mortar preponderates in the community. This paper explores the suitability of emerging cementitious resins as part of retrofit technologies, including polyester-silica, ultra-high performance concrete (UHPC), and geopolymer. Accompanied by the rheological and mechanical characteristics of these resins, the performance of reinforced concrete beams strengthened with NSM CFRP is studied with the aim of elucidating flexural capacities, displacements, and failure modes. To reflect realistic circumstances, the beams are damaged by stochastically simulated corrosion. Analytical modeling accounts for the pertinence of existing design approaches and renders a practice protocol with a modification factor.

9. RESEARCH SIGNIFICANCE

In an effort to advance the state of the art, the relevance of non-conventional bonding agents is examined for the NSM method. The interaction between the cementitious resins and CFRP strips, which is inherent in the fundamental mechanics of the retrofit system, plays an important role in governing the behavior of the strengthened beams. Through the acquaintance gained from the experimental program combined with theoretical modeling, an obscure facet is construed in the discipline of NSM CFRP. The proposed design recommendations allow for a broad range of damage levels paired with a cross-sectional loss in steel reinforcement, equivalent to 100 years of pitting corrosion. Recognizing the propitious opportunity and technical competency of the inorganic resins brings to light the cutting-edge research of structural rehabilitation and will eventually constitute a section in practice guidelines.

10. SIMULATION OF CORROSION DAMAGE

A benchmark bridge deck was designed to simulate the ramifications of corrosion under an aggressive service environment [Figure II1(a)]. The thickness of the deck was 250 mm (10 in.) with a strip width of 1 m (3.3 ft), which was reinforced by No. 4 bars (12.7 mm [0.5 in.] in diameter) at a cover depth of 63.5 mm (2.5 in.). Below is a description on the initiation and progression of corrosion damage.

10.1 Corrosion Initiation

Equation II1 predicts the initiation of corrosion (t_i) in years (Thoft-Christensen et al. 1996)

$$t_i = \frac{C^2}{4D_c}\left[erf^{-1}\left(\frac{C_{cr}-C_0}{C_i-C_0}\right)\right]^{-2} \tag{II1}$$

where C is the concrete cover in cm; D_c is the diffusion coefficient in cm^2/sec; *erf* is the Gauss error function; and C_{cr}, C_0, and C_i are the critical, equilibrium, and initial chloride concentrations, respectively. According to published papers, the following properties were taken: $D_c = 1\times10^{-8}$ cm^2/s (1.55×10^{-9} in.^{2}/s) for a bridge member exposed to corrosive environments (Saugues 2003), C_{cr} = 0.4% and C_i = 0% (percent-weight of the cement) (Elsener and Angst 2016), and C_0 = 1.6% (Thoft-Christensen et al. 1996).

10.2. Pitting Corrosion

The pitting depth of the reinforcement [p_{pit} in Figure II1(b)] may be calculated by

$$p_{pit}(t) = \alpha_p\left(\frac{1}{2}\left(\phi_0 - \phi_{t_p}(t)\right)\right) \tag{II2}$$

where α_p is the pitting factor (α_p = 4, Cao and Cheung 2014); and ϕ_0 and ϕ_{t_p} are the diameters of the initial and damaged rebars, respectively. The reduced diameter of the steel is estimated using (Vu and Stewart 2000; Ahmad 2006)

$$\phi_{t_p}(t) = \phi_0 - r_{corr}(t_p)t_p \tag{II3}$$

$$r_{corr}(t_p) = C_c\frac{W_a i_{corr}(t_p)}{n\rho} \tag{II4}$$

$$i_{corr}(t_p) = \frac{37.8(1-w/c)^{-1.64}}{C}k_1 t_p^{k_2} \tag{II5}$$

where t_p is the corrosion time in years ($t_p = t_{current} - t_i$); C_c is a conversion factor (C_c = 0.00327 for mm/year); W_a is the atomic weight of iron (W_a = 55.9 g/mol (0.12 lb/mol)); $i_{corr}(t_p)$ is the corrosion current density in μA/cm^2; n is the number of electrons in iron (n = 2 for $Fe \rightarrow Fe^2 + 2e$); ρ is the density (7 g/cm^3 (0.25 lb/in.^{3})); w/c is the water-to-cement ratio in concrete; and k_1 and k_2 are constants (k_1 = 0.85 and k_2 = -0.3 after one year of corrosion initiation). The width of the pitted portion [$a_{pit}(t)$, Figure II1(b)] is

$$a_{pit}(t) = 2p_{pit}(t)\sqrt{1-\left(\frac{p_{pit}(t)}{\phi_0}\right)^2} \tag{II6}$$

The time-dependent pitting and width ratios of the rebar [$R_p(t)$ and $R_w(t)$, respectively] are defined as

$$R_p(t) = \frac{p_{pit}(t)}{\phi_0} \tag{II7}$$

$$R_w(t) = \frac{a_{pit}(t)}{\phi_0} \tag{II8}$$

Upon determining $R_p(t)$ and $R_w(t)$, the attributes of pitting corrosion in any rebar size at time t ($p_{pit}(t)$ and $a_{pit}(t)$) can be attained.

10.3 Monte-Carlo Simulation

Because corrosion characteristics are intrinsically stochastic in a concrete structure, the formulated models were simulated by the Monte-Carlo method. This numerical technique generates possible outcomes based on random sampling, which is suitable for solving complex engineering problems with uncertainty (Coolen et al. 2021). The statistical properties and distribution types enumerated in Table II1 were substituted into Eqs. 1 to 5 for the inference of corrosion initiation years and the $R_p(t)$ and $R_w(t)$ ratios up to a service period of 100 years, employing over 50,000 samples.

10.4 Pitting Corrosion

Figures II2(a) and (b) display the simulated corrosion initiation years and pitting ratios of the benchmark bridge deck, respectively (selected cases are visible for brevity). The density of the data was concentrated within a certain range, albeit scattered, which means that representative values with high occurrence probability can be identified for each parameter. The predicted corrosion initiation time of 20.5 years [Figure II2(a)], on average, was reasonably close to a reported period of 20 to 30 years (Stewart et al. 2004; FHWA 2011). As shown in Figure II2(b), with the increased service year, the extent of deviation was enlarged in the pitting ratio due to accumulated uncertainties. The average pitting and width ratios of the reinforcement after the onset of corrosion are charted in Figs. II2(c) and (d), respectively. The magnitudes of these ratios noticeably went up between 25 and 50 years, pointing out the active progression of corrosion. Literature states that piled rust retards the ingress of oxygen when significant corrosion develops (Yuan et al. 2010), thereby decelerating electrochemical reactions necessary for the pitting damage.

11. LABORATORY EXPERIMENT

A test program is delineated to outline material properties, specimen preparation, retrofitting schemes, and instrumentation. For material- and structure-level investigations, mechanical and rheological techniques are utilized.

11.1 Materials

The specified compressive strength of ready-mix concrete was f'_c = 25 MPa (3,630 psi). Five cylinders (100 mm [4 in.] in diameter by 200 mm [8 in.] in depth) were tested per ASTM C39 (ASTM 2018), and the average 28-day strength of the cylinders was found to be 27 MPa (3,920 psi). The yield strength and elastic modulus of Grade 60 steel reinforcing bars were f_y = 414 MPa (60 ksi) and E_s = 200 GPa (29,000 ksi), respectively. Prefabricated CFRP strips with a dimension of 2 mm (0.08 in.) in thickness and 16 mm (0.63 in.) in width were the primary strengthening material, comprising high-strength carbon fibers and an epoxy resin. The unidirectional composite strips possessed a tensile strength of f_{fu} = 2,068 MPa (300 ksi) and corresponding modulus of E_f = 124 GPa (18,000 ksi) with an ultimate strain of ε_{fu} = 0.017. The textured surface of this commercial product enhances the bond against an adhesive. Three types of cementitious resins were employed as a bonding agent: polyester-silica, UHPC, and geopolymer. For the production of polyester-silica, a catalyst was added to a polyester liquid and the chemically reactive solution was mixed with silica sand at a ratio of 20% and 80% by mass, respectively. The silica had an SiO_2 content of 90.3% with a particle size of 0.45 mm (0.018 in.). The non-shrink UHPC mixture was composed of particle-optimized ingredients along with carbon nano fibers (detailed information is not reported owing to contractual obligations). As guided by the manufacturer's manual, a paste and a deformer were blended with tap water in a mixer for two minutes; then, packaged dry powers were added and stirred for additional six minutes until a homogeneous grout was achieved. Geopolymer was an aluminosilicate matrix with the succeeding nominal properties: a set time of 60 minutes (ASTM C807, ASTM 2020a), a 28-day shrinkage of 0.07% (ASTM C1090, ASTM 2015b), a chloride penetration of 60 mm (2.4 in.) at 90-day ponding (ASTM C1543, ASTM 2010), and a freeze-thaw loss of 0% at 300 cycles (ASTM C666, ASTM 2015a).

11.2 Specimens

Pitting corrosion—The stochastic model described above was implemented to replicate pitting corrosion in steel reinforcement (No. 3 bars). Multiplying the diameter of ϕ_0 = 9.53 mm (0.375 in.) by the simulated pitting and width ratios (Figure II2), corrosion damage was estimated from 25 to 100 years [Figure II3(a)]. Three spots, targeted near the middle of each rebar, were cut using a high-precision computer-numeric-control milling machine [Figure II3(b)].

Cubes and beams—Referring to ASTM C109 (ASTM 2020), 15 cubes (50 mm [2 in.], each side) were cast with the cementitious resins and moisture-cured under a relative humidity of 99% for 14 days. Reinforced concrete beams were prepared with a dimension of 165 mm (6.5 in.) in width by 100 mm (4 in.) in depth by 1,200 mm (4 ft.) in length. The machined No. 3 rebars were located at an effective depth of 70 mm (2.75 in.), as depicted in Figure II3(c), and No. 2 shear stirrups (6.35 mm [0.25 in.] in diameter) were placed at spacings of 75 mm (3 in.) to ensure flexural failure. A Styrofoam strip (900 mm [35 in.] long) was positioned underneath the steel cage for the installation of NSM CFRP and then concrete was poured.

11.3 Strengthening Plan

After 28 days of curing in an environmental chamber at a 99% relative humidity and 23°C (73°F), all beams were taken out, cleaned with an airbrush, washed, and fully dried. The groove of the beams, created by the Styrofoam, was ground using a knotted-wire steel wheel to improve the bond against the cementitious resins. It should be noted that the groove size of 25 mm (1 in.) deep and 13 mm (0.5 in.) wide complied with the provision of ACI 440.2R-17 (ACI 2017). The inorganic resins were mixed as explained earlier and applied to around 70% of the groove depth; afterward, a single piece of CFRP (900 mm [35 in.] long) was firmly inserted and the remaining portion of the groove was filled. In line with the findings of preliminary testing on the strength of the resins (i.e., the strength converged after 14 days), the CFRP-bonded beams were additionally cured for 14 days. Table II2 imparts the identification of the prepared beams, depending upon the type of resin and the simulated time of corrosion. For example, the P75 specimen indicates that a beam suffering 75 years of corrosion was CFRP-strengthened with polyester-silica. It is worth noting that unstrengthened beams were not tested since the focus of the study was on exploring the performance of the cementitious resins.

11.4 Test Methods

Compressive strength—The previously-mentioned cylinders and cubes were monotonically compressed to obtain the strength of the concrete and resins [Figs. II4(a) and (b)].

Workability—Given that the morphological nature of the cementitious resins differs from that of conventional epoxies when filling a narrow groove, workability was regarded to be crucial. A vane shear test was performed to measure the rheology of the three resin types [Figure II4(c)]. Cylindrical containers (45 mm [1.8 in.] in diameter and 100 mm [4 in.] in depth) were filled with the individual resins, and the inserted vane (12.7 mm [0.5 in.] in width and 12.7 mm [0.5 in.] in height) was rotated at 0.1 revolutions per minute for 60 minutes. Strain rates were acquired (details will be described) for the appraisal of angular velocities that would quantify the resins' applicability to NSM CFRP.

Flexure—The strengthened beams were loaded under four-point bending at a rate of 1 mm (0.0394 in.)/min. [Figure II4(d)]. The simply-supported beams were instrumented with a load cell and a linear potentiometer at midspan to record the applied load and the displacement, respectively. Strain transducers, customarily called PI gages, were mounted at a distance of 25 mm (1 in.) from the top and bottom of the beams for monitoring compressive and tensile deformations, respectively.

12. RESULTS AND DISCUSSION

The outcomes of laboratory testing are gleaned and analyzed with an emphasis on the practicality of cementitious resins as a bonding agent for NSM CFRP strips. Of interest are the flexural responses of retrofitted beams with pre-damage and the feasibility of the resins.

12.1 Properties of Cementitious Resins

Figure II5(a) summarizes the compressive strength of the cementitious resins. The average 14-day strength of 34.4 MPa (4,989 psi) in polyester-silica was higher than the 28-day strength of the concrete (27 MPa [3,920 psi]). This illustrates that cross-linked monomers, stemming from the condensation reactions of the resin (Vargas et al. 2012), were more efficacious compared with the load-bearing of the coarse aggregates. It is also known that the strong bond between the polyester and silica was accomplished by mutual engagement through the rough interfacial surfaces (Sudirman et al. 2012). The strength of UHPC reached over 115 MPa (16,679 psi), which was ascribed to the prompt hydration associated with the fine binder particles and tricalcium silicate (Neville 1995). From a mechanical standpoint, the carbon nano fibers in the UHPC mixture induced the so-called bridging effect that precluded the formation of microcracks (Meng and Khayat 2018). The strength of the geopolymer resin was 21 MPa (3,045 psi); prior research clarifies that the dissolution of aluminum and silicon and the polycondensation with metallic minerals were instrumental in resisting external loadings (Xu and Van Deventer 2000).

Figure II5(b) shows an assessment on the resins' workability. The angular change of the vane ($\Delta\theta$) was logged and converted to a shear stress using (Bauer et al. 2007)

$$\tau = \frac{K\Delta\theta}{\pi\left(\frac{D^2H}{2}+\frac{D^3}{6}\right)} \tag{II9}$$

where τ is the shear stress of the fresh resin, equivalent to the rotational resistance of the vane; K is the spring constant (1.85 Nmm [0.016 lb-in.] per angular change); and D and H are the width and depth of the vane, respectively. The shear stress of polyester-silica was 340 Pa (6.8 lb/ft^2), which was 175% and 507% higher than those of UHPC and geopolymer, respectively. The inset of Figure 5(b) reveals the viscosity of the resins with respect to strain rate. In accordance with the theory of Newtonian fluids (Ramsey 2019), the viscosity of an amorphous material is defined as the ratio of shear stress to strain rate ($\Delta\theta$ per unit time). To gain a viscosity of 494 kPa-s/rad (0.07 ksi-s/rad) during the test period of 60 minutes, polyester-silica required a strain rate of 688 rad/s; contrarily, UHPC and geopolymer necessitated 393 rad/s and 135 rad/s, respectively. In other words, the internal friction of polyester-silica was much higher and thus its workability was concluded to be the least favorable among the three resins.

12.2 Capacity

The ultimate load of the test beams is graphed in Figure II6(a). The flexural capacity of the strengthened beam with polyester-silica at a simulated corrosion period of 25 years (P25 in Table II2) was 47.0 kN (10.6 kips), whereas the capacities of the beams with UHPC (U25) and geopolymer (G25) were 40.5 kN (9.1 kips) and 38.5 kN (8.7 kips), respectively. This tendency was maintained irrespective of the corrosion time, leading to the fact that the polyester-silica resin outperformed other types. Furthermore, it was substantiated that the strength of the cementitious resins [Figure II5(a)] was not directly proportional to the functionality as a bonding agent for NSM CFRP application. The implications of the corrosion

damage are described in Figure II6(b) where the time-dependent capacities are normalized by the 25-year capacities belonging to the individual resins. The load drop ratio of the beams with UHPC consistently dwindled up to 100 years: 4.96% (25 to 50 years), 2.31% (50 to 75 years), and 0.79% (75 to 100 years). Regarding the beams with polyester-silica and geopolymer, the variation of the load ratios was akin, and conspicuous reductions were noticed beyond 50 years. For instance, the drop ratios of the beams with geopolymer were 0.73% (25 to 50 years) and 11.6% (50 to 75 years). It is hence stated that the UHPC resin interacted better with the residual cross-sectional area of the corrosion-damaged steel reinforcement and demonstrated reliable long-term performance; specifically, the high-strength UHPC effectively distributed tensile stresses to those rebars and alleviated strain localizations.

12.3 Flexural Behavior

Figure II7(a) exhibits the load-displacement relationship of the UHPC-bonded beams. The declined pre-yield slope with an increase in corrosion year signifies that the narrow CFRP strip did not appreciably upgrade the serviceability of the beams. Technically speaking, the transformed CFRP area accounted for 3.6% to 4.0% of the cracked concrete sections with a modular ratio of $n_f = 5.05$; that is, $n_f A_f = 161$ mm^2 (0.25 in.^{2}) vs. $A_{ct} = 4{,}482$ mm^2 (6.95 in.^{2}) and 4,020 mm^2 (6.23 in.^{2}) at 25 and 100 years, respectively, where A_f is the cross-sectional area of CFRP and A_{ct} is the area of the cracked concrete section, respectively. The yield load of the beams was a function of corrosion due to the reduced steel areas, and the fluctuating yield plateaus imply that the UHPC resin fractured periodically (supplementary discussions will be given). As the damage level rose, the breadth of the plateaus enlarged, which is attributable to the lowered steel-reinforcement ratio: $\rho_s = 1.22\%$ and 0.86% at 25 and 100 years, respectively, in which $\rho_s = A_s/(bd)$ where A_s is the steel area, b is the beam width, and d is the effective depth of the beam. The effects of the resin type are plotted in Figure II7(b) at a selected period of 50 years. The response of all beams was virtually identical until a load of 23.4 kN (5.3 kips); then, a bifurcation was noted in the beam with geopolymer (G50). Unlike the case of the U50 and G50 beams, the P50 beam showed an abrupt load drop. Care should thus be exercised when adopting polyester-silica for strengthening purposes. The archetypal development of compressive and tensile strains under flexural loading was logged [Figure II7(c)]; however, meaningful comparisons were not available since several readings were corrupted (concrete cracks traversed the installation points of the PI gages). By numerically integrating the load-displacement curves, the energy of the beams that dissipated up to the peak loads was quantified and is charted in Figure II7(d). The increased corrosion years lessened the energy levels in all categories. While the use of geopolymer significantly raised the energy dissipation capability, the resin's efficacy plummeted after 50 years. Considering that volume changes and grain friction dominate the inelastic energy dissipation of geopolymer (Akono et al. 2019), the decreased steel reinforcement ratios in the G75 and G100 beams appeared to influence the deformational characteristics of the resin.

12.4 Failure Mode

General pattern—The failure modes of the test beams are pictured in Figure II8. Although concrete crushing caused the ultimate limit state of all beams in conjunction with flexural and shear cracks, the degree of corrosion and the retrofit schemes also affected failure mechanisms. The UHPC-bonded beams at 25 and 50 years [U25 and U50 in Figure II8(a), respectively] displayed regional failure; on the other hand, those at 75 and 100 years [U75 and U100 in Figure II8(a), respectively] showed distributed cracks along the loading span. This fact denotes that the applied bending moment spread with a decrease in the beam's reinforcement ratio ($\rho_s = 1.22\%$ at 25 years vs. $\rho_s = 0.86\%$ at 100 years). Such a trend was also observed in the beams with polyester-silica [P25 and P100 in Figure II8(b)], which was different from the beams with geopolymer [G25 and G100 in Figure II8(b)] that failed with a few vertical cracks.

Interfacial aspect—The interface between the concrete substate and CFRP is seen in Figure II9. Regardless of corrosion time, the integrity of the retrofit system was preserved in the UHPC-bonded beams [U25 and U100 in Figs. II9(a) and (b), respectively]. The recurrent crack spacings and the fractured resin were responsible for the oscillating yield plateaus that were articulated in Figure II7(a). The tensile soffit of the system alongside polyester-silica [P100, Figure II9(c)] was analogous to the foregoing cases, except for the several secondary cracks. Contrary to these groups, debonding was spotted in the geopolymer beam after the crushing of the concrete [Figure II9(d)]. The far-right diagonal tension crack near the support (dotted circle) coupled with the relatively weak resin brought about a geometric discontinuity and precipitated the bond failure.

13. MODELING

Analytical models are formulated to comprehend the degree of stress transfer from a concrete substrate to CFRP strips, dependent upon the type of cementitious resins. Upon examining the adequacy of traditional design approaches, a modification factor is suggested to properly accommodate the repercussions of such resins for an NSM-strengthening system.

13.1 Assessment of ACI 440.2R-17

Two possible failure classes are stated in ACI 440.2R-17 (ACI 2017): i) concrete crushing at the maximum usable strain of $\varepsilon_{cu} = 0.003$, and ii) CFRP debonding at $\varepsilon_{fd} = 0.7\varepsilon_{fu}$ for an NSM system. Assuming that plane sections remain plane (complete composite action) and force equilibrium is satisfied, sectional analysis may be conducted to predict the ultimate load of the test beam with the CFRP strip (P_u) subjected to concrete-crushing ($\varepsilon_c = \varepsilon_{cu}$, in which ε_c is the concrete strain at the top of the beam)

$$P_u = \frac{2\left(M_{ns} + M_{nf}\right)}{a} \tag{II10}$$

$$M_{ns} = A_s f_y \left(d - \frac{\beta c}{2} \right) \tag{II11}$$

$$M_{nf} = A_f f_f \left(d_f - \frac{\beta c}{2} \right) \tag{II12}$$

where M_{ns} and M_{nf} are the nominal moment resistance of the steel and CFRP components, respectively; β is the stress block factor; c is the neutral axis depth; f_f is the CFRP stress; and d_f is the distance from the extreme compression fiber of the beam to the centroid of the CFRP strip. In the event of debonding ($\varepsilon_c < \varepsilon_{cu}$), the resultant compressive force of the concrete can be estimated by the equivalent rectangular block with (ACI 2017)

$$\alpha_1 = \frac{3\varepsilon_c^{'}\varepsilon_c - \varepsilon_c^2}{3\beta_1\left(\varepsilon_c^{'}\right)^2} \tag{II13}$$

$$\beta_1 = \frac{4\varepsilon_c^{'} - \varepsilon_c}{6\varepsilon_c^{'} - 2\varepsilon_c} \tag{II14}$$

$$\varepsilon_c^{'} = \frac{1.7 f_c^{'}}{E_c} \tag{II15}$$

where α_1 and β_1 are the empirical factors; and E_c is the elastic modulus the concrete ($E_c = 57{,}000\sqrt{f_c^{'}}$ in psi and $4{,}730\sqrt{f_c^{'}}$ in MPa, ACI 2019). Figure I10(a) shows the calculated concrete and CFRP strains pursuant to the provisions of ACI 440.2R-17 (ACI 2017) when the retrofitted section failed. The invariant CFRP strains gradually ascended after the initiation of corrosion, and the strain levels appertaining to the debonding scenario was 22.2% lower than those to the crushing condition, on average. The concrete

strains related to the debonding failure were almost constant because the increased steel strains, resulting from the corrosion damage, were offset by the shortened neutral axis depth. As shown in Figure II10(b), the load-carrying capacity of the retrofitted beam steadily diminished over time, including an average difference of 11.0% between the compression- and tension-controlled sections. Figures II10(c) and (d) evaluate the applicability of the ACI 440.2R-17 method. The flexural capacity of the beam with polyester-silica was 11.3% lower than the full capacity estimated by ACI 440.2R-17 [concrete crushing in Figure II10(c)], on average, followed by 20.2% and 25.9% for the beams with UHPC and geopolymer, respectively. The discrepancy decreased for the tension-controlled section [Figure II10(d)]; the average load ratios of the crushing and debonding were 0.81 [Figure II10(c)] and 0.91 [Figure II10(d)], respectively. Overall, the ACI 440.2R-17 approach needs to be revised for the capacity prediction of NSM CFRP bonded with the cementitious resins, particularly when the strengthened beam fails by concrete-crushing.

13.2 Effective Stress Factor

Principle—As elaborated earlier, the theoretical capacity of the retrofitted section with full composite action overestimated the ultimate load of the test beams. It is rational to conjecture that the applied tensile stresses were in part transferred to the CFRP strip through the inorganic medium; scilicet, the local deformation of the cementitious resins, dissipated interfacial energy (Abrishambaf et al. 2017) and mitigated the development of tensile forces in the strip, which brought down the effectiveness of CFRP-strengthening. To handle such inconsistency, an effective stress factor (Ω) was proposed for the execution of the sectional analysis, and Eq. II12 was replaced by Eq. II16

$$M_{nf} = A_f f_{fe}\left(d_f - \frac{\beta c}{2}\right) \tag{II16}$$

$$f_{fe} = \Omega f_f = \Omega E_f \varepsilon_f \tag{II17}$$

where f_{fe} is the effective stress of CFRP or the fraction of the CFRP stress from the sectional analysis. This concept is similar to the strain reduction factor in prestressed concrete with unbonded tendons (Naaman et al. 2002). The Ω factor was calibrated through iterating Eq. II10 with assumed c and Ω values until the predicted capacity was equal to its experimental counterpart. Even if CFRP-debonding was not considered herein, because concrete crushing was the primary source of failure in all test beams, the same procedure can be adopted with Eqs. II13 to II15 when determining the Ω factor for tension-controlled sections.

Implementation—Figure II11(a) compares CFRP strains obtained from the iterative approach (ε_f[cementitious resin]) and the conventional sectional analysis (ε_f[composite action]). On all occasions, the strain ratios were lower than unity, reaffirming the aforementioned partial composite action for the cementitious resins. The strain ratios of the beams with polyester-silica were higher than the ratios of other beams; however, the former was more susceptible to corrosion damage with a drop of 16.4% between 50 and 75 years. Figure II11(b) shows the collected effective stress factors. Aligning with the propensity of the strain ratios, the stress transfer of polyester-silica was superior to that of UHPC and geopolymer (average Ω factor = 0.70 vs. 0.47 vs. 0.36).

Appraisal—To address potential concerns arising from the limited number of the experimental specimens, Monte-Carlo simulations were carried out employing the Ω-based sectional analysis with the statistical properties listed in Table II1. The calibrated effective stress factors were considered to be deterministic, and all other variables were modeled as stochastic parameters. Typical predictions for the beams with polyester-silica at 25 and 100 years are visible in Figure II11(c). Notwithstanding the scatter of the computed load-carrying capacities, the absolute margin of error was less than 2.0% between the test and simulation [Figure II11(d)].

Design proposal—In view of the preceding evaluations, the effective stress factors were linked with the corrosion levels and recommendations were made in Table II3. For practical reasons, the factors were rounded, and three damage categories were defined (moderate, significant, and critical), contingent upon the loss of cross-sectional area in the steel reinforcement. The proposed Ω factors, spanning from 0.30 to 0.80, were intended to be conservative since i) the scope of the present research was restrictive, and ii) there would be numerous uncertainties in existing concrete members.

14. SUMMARY AND CONCLUSIONS

This report has dealt with the relevance of cementitious resins for strengthening reinforced concrete beams with NSM CFRP strips. Three types of emerging resins were taken into consideration: polyester-silica, UHPC, and geopolymer. A wide variety of corrosion intensity was numerically simulated up to 100 years and representative damage levels were chosen for laboratory testing. A total of 12 strengthened beams were loaded under four-point bending, and their load-carrying capacity, displacement, and failure modes were investigated. Additionally, the resins' workability was measured to understand the rheological suitability as a bonding agent for NSM application. As per the findings of the experimental program in tandem with stochastic modeling, design recommendations were suggested. Contemplating that the scope of the research was rather narrow, and the number of test specimens was limited, the proposal may be improved by the continuation of a comprehensive study. The following conclusions are drawn:

- There was no correlation between the compressive strength and the rheological resistance of the resins; the workability of polyester-silica showing a strength of 34.4 MPa (4,989 psi) was adverse relative to that of UHPC and geopolymer (compressive strength = 115 MPa [16,679 psi] and 21 MPa [3,045 psi], respectively). Nonetheless, all these resins were appropriate bonding agents that filled the 13-mm (0.5-in.) wide groove of the beams without difficulty.
- Throughout the simulated corrosion period of 100 years, the strengthened beams with polyester-silica demonstrated consistently higher capacities than the beams with other resins. In contrast to the gradually declining capacity of the UHPC-bonded beams with time, the capacity degradation of the polyester-silica- and geopolymer-bonded beams revealed an abrupt transition between 50 and 75 years. Special attention should therefore be paid when retrofitting aged concrete members suffering a substantial loss of steel reinforcement of 10% or more.
- The NSM system did not improve the serviceability of the upgraded beams owing to the marginal influence of the CFRP strip on the transformed concrete section being less than 4.0%. The resin configurations altered the post-yield behavior of the beams. As the level of corrosion rose, the dissipation of flexural energy (up to the peak loads) decreased, in particular for the geopolymer-bonded beams.
- While the cracking pattern of the beams with UHPC and polyester-silica was reliant upon the corrosion year (regional cracking at 25 years vs. distributed cracking at 100 years), the beams with geopolymer steadily exhibited localized cracking. The integrity of the CFRP-resin interface was retained until the concrete-crushing failure took place.
- The provisions of ACI 440.2R-17 (ACI 2017) overestimated the capacity of the strengthened beams with the cementitious resins over 25%. The hypothetical capacities of these beams related to the compression- and tension-controlled sections differed by 12%. With the aim of refining capacity-prediction outcomes, the effective stress factor (Ω) was calibrated and recommended for practices; when deciding the Ω factor ranging from 0.30 to 0.80, the resin type and expected damage level prior to applying the retrofit system should be taken into consideration.

15. REFERENCES

Abrishambaf, A., Pimentel. M., and Nunes, S. 2017. “Influence of fibre orientation on the tensile behaviour of ultra-high performance fibre reinforced cementitious composites,” *Cement and Concrete Research*, 97, 28-40.

ACI. 2010. *Guide for the Design and Construction of Externally Bonded Fiber-Reinforced Polymer Systems for Strengthening Unreinforced Masonry Structures* (ACI 440.7R-10), American Concrete Institute Committee 440, Farmington Hills, MI.

ACI. 2017. *Guide for the Design and Construction of Externally Bonded FRP Systems for Strengthening Concrete Structures* (ACI 440.2R-17), American Concrete Institute Committee 440, Farmington Hills, MI.

ACI. 2019. *Building Code Requirements for Structural Concrete and Commentary* (ACI 318-19), American Concrete Institute, Farmington Hills, MI.

Ahmad, Z. 2006. *Principles of Corrosion Engineering and Corrosion Control,* Butterworth-Heinemann, Oxford, UK.

Akono, A.T., Koric, S., and Kriven, W.M. 2019, “Influence of pore structure on the strength behavior of particle- and fiber-reinforced metakaolin-based geopolymer composites,” *Cement and Concrete Composites*, 104, 103361.

Al-Saadi, N.T.K., Mohammed, A., and Al-Mahaidi, R. 2017, “Assessment of residual strength of concrete girders rehabilitated using NSM CFRP with cementitious adhesive made with graphene oxide after exposure to fatigue loading,” *Construction and Building Materials*, 153, 402-422.

Aprile, A., and Monti, G. 2022. “Advanced Methods for Structural Rehabilitation,” *Buildings*, 12(1), 79.

ASTM. 2010. “Standard test method for determining the penetration of chloride ion into concrete by ponding” (ASTM C1543), American Society for Testing and Materials, West Conshohocken, PA.

ASTM. 2015a. “Standard test method for resistance of concrete to rapid freezing and thawing” (ASTM C666), American Society for Testing and Materials, West Conshohocken, PA.

ASTM. 2015b. “Standard test method for measuring changes in height of cylindrical specimens of hydraulic-cement grout” (ASTM C1090), American Society for Testing and Materials, West Conshohocken, PA.

ASTM. 2018. “Standard test method for compressive strength of cylindrical concrete specimens” (ASTM C39), American Society for Testing and Materials, West Conshohocken, PA.

ASTM. 2020a. “Standard test method for time of setting of hydraulic cement mortar by modified vicat needle” (ASTM C807), American Society for Testing and Materials, West Conshohocken, PA.

ASTM. 2020b. “Standard test method for compressive strength of hydraulic cement mortars (using 2-in. or [50 mm] cube specimens)” (ASTM C109), American Society for Testing and Materials, West Conshohocken, PA.

Atadero, R.A., and Karbhari, V.M. 2008. “Calibration of resistance factors for reliability based design of externally-bonded FRP composites,” *Composites Part B*, 39, 665-679.

Baji, H., and Ronagh, H.R. 2016. “Reliability-based study on ductility measures of reinforced concrete beams in ACI 318,” *ACI Structural Journal*, 113(2), 373-382.

Bauer, E., de Sousam J.G.G., Guimaraes, E.A., and Silva, F.G.S. 2007. “Study of the 525 laboratory Vane test on mortars,” *Building and Environment*, 42, 86-92.

Cao, C., and Cheung, M.M.S. 2014. “Non-uniform rust expansion for chloride-induced pitting corrosion in RC structures,” *Construction and Building Materials*, 51, 75-81.

Cao, X.-Y., Wu, G., and Ju, J.-W.W. 2022. “Seismic performance improvement of existing RCFs using external PT-PBSPC frame sub-structures: Experimental verification and numerical investigation,” *Journal of Building Engineering*, 46, 103649.

Chung, P.-T., and Chou, C.-C. 2022. “One-sided shear retrofit of reinforced concrete beams in existing high-rise buildings,” *Engineering Structures*, 252, 113634.

Coolen, F.P.A., De Bock, J., and Aslett, L.J. 2021. *Uncertainty in Engineering—Introduction to Methods and Applications*, Springer, Cham, Switzerland.

De Lorenzis, L., and Teng, J.G. 2007. “Near-surface mounted FRP reinforcement: An emerging technique for strengthening structures,” *Composites Part B*, 38, 119-143.

Elsanadedy, H.M., Abbas, H., Almusallam, T.H., Al-Salloum, Y.A. 2019. “Organic versus inorganic matrix composites for bond-critical strengthening applications of RC structures: state-of-the-art review,” *Composites Part B*, 174, 106947.

Elsener, B., and Angst, U. 2016. “Corrosion inhibitors for reinforced concrete,” *Science and Technology of Concrete Admixtures*, 321-339.

FHWA. 2011. “Multiple corrosion-protection systems for reinforced concrete bridge components, Report No. FHWA-HRT-11-060,” Federal Highway Administration, Washington, D.C.

Fox, M., Trost, S., and Hellman, S. 2007. “Evaluation of Novel Methods to Measure Water-to-Cement Ratio of Fresh Concrete, Final Report For Highway IDEA Project 105,” Transportation Research Board, Washington, D.C.

Grande, E., and Milani, G. 2021. “Numerical study of the bond behavior of DMF systems,” *Structures*, 31, 921-939.

Kim, S., Frangopol, D.M., and Zhu, B. 2011. “Probabilistic optimum inspection/repair planning to extend lifetime of deteriorating tsructures,” *Journal of Performance of Constructed Facilities*, 25(6), 534-544.

Kuntal, V.S., Chellapandian, M., Prakash, S.S., and Sharma, A. 2020. “Experimental study on the effectiveness of inorganic bonding materials for near-surface mounting shear strengthening of prestressed concrete beams,” *Fibers*, 8(6), 40.

Labo, S., Passoni, C., Marini, A., and Belleri, A. 2020. “Design of diagrid exoskeletons for the retrofit of existing RC buildings,” *Engineering Structures*, 220, 110899.

Li, C.Q., and Melchers, R.E. 2005. “Time-dependent risk assessment of structural deterioration caused by reinforcement corrosion,” *ACI Structural Journal*, 102(5), 754-762.

Meng, W., and Khayat, K.H. 2018. “Effect of graphite nanoplatelets and carbon nanofibers on rheology, hydration, shrinkage, mechanical properties, and microstructure of UHPC,” *Cement and Concrete Research*, 105, 64-71.

Mirza, S.A., Kikuchi, D.K., and MacGregor, J.G. 1980. “Flexural strength reduction factor for bonded prestressed concrete beams,” *ACI Journal*, 77(4), 237-246.

Naaman, A. E., Burns, N., French, C., Gamble, W. L., and Mattock, A. H. 2002. “Stresses in unbonded prestressing tendons at ultimate: recommendation,” *ACI Structural Journal*, 99(4), 520-531.

Nowak, A.S., and Collins, K.R. 2013. *Reliability of Structures* (Second Edition), CRC Press, Boca Raton, FL.

Neville, A.M. 1995. *Properties of Concrete* (Fourth Edition), Prentice Hall, Essex, UK.

Okeil, A., El-Tawil, S., and Shahawy, M. 2002. “Flexural reliability of reinforced concrete bridge girders strengthened with carbon fiber-reinforced polymer laminates,” *Journal of Bridge Engineering*, 7(5), 290-299.

Ramsey, M.S. 2019. “Rheology, viscosity, and fluid types,” *Practical Wellbore Hydraulics and Hole Cleaning*, 217-237.

Reddy, G.R. 2022. “On structural rehabilitation and retrofitting for risk reduction,” *Civil Engineering for Disaster Risk Reduction*, 373-381, *Springer Tracts in Civil Engineering*, New York, NY.

Sagues, A.A. 2003. “Modeling the effects of corrosion on the lifetime of extended reinforced concrete structures,” *Corrosion*, 59(10), 854-866.

Stewart, M.G., and Rosowsky, D.V. 1998. “Time-dependent reliability of deteriorating reinforced concrete bridge decks,” *Structural Safety*, 20, 91-109.

Stewart, M.G., Estes, A.C., and Frangopol, D.M. 2004. “Bridge deck replacement for minimum expected cost under multiple reliability constraints,” *Journal of Structural Engineering*, 130(9), 1414-1419.

Sudirman, Anggaravidya, M., Budianto, E., and Gunawan, I. 2012. “Synthesis and characterization of polyester-based nanocomposite,” *Procedia Chemistry*, 4, 107-113.

Thoft-Christensen, P., Jensen, F.M., Middleton, C.R., and Blackmore, A. 1996. “Assessment of the reliability of concrete slab bridges,” 7th IFIP WG 7.5 Working Conference, Boulder, CO, 1-8.

Val, D.V., and Stewart, M.G. 2003. “Life-cycle cost analysis of reinforced concrete structures in marine environment,” *Structural Safety*, 25, 343-362.

Vargas. M.A., Sachsenheimer, K., and Guthausen, G. 2012. “In-situ investigations of the curing of a polyester resin,” *Polymer Testing*, 31, 127-135.

Vu, K.A.T., and Stewart, M.G. 2000. “Structural reliability of concrete bridges including improved chloride-induced corrosion models,” *Structural Safety*, 22, 313-333.

Xu, H., and Van Deventer, J.S.J. 2000. “The geopolymerisation of alumino-silicate minerals,” *International Journal of Mineral Processing*, 59, 247-266.

Xue, W., Tan, Y., and Peng, F. 2020. “Experimental study on damaged prestressed concrete beams using external post-tensioned tendons,” *ACI Structural Journal*, 117(1), 159-168.

Yang, S., Wang, S., Fang, X., and Tao, Y. 2015. “Bond performance between NSM FRP rods and concrete using ECC as bonding materials,” Proceedings of the Second International Conference on Performance-based and Life-cycle Structural Engineering (PLSE 2015), 490-495.

Yu, J.-G., Cheng, L., Liu, S., Fu, B., Li, B. 2021. “Inorganic adhesive based near-surface-mounted fibre reinforced polymer for strengthening of concrete structures: an overview,” *Structures*, 33, 2099-2120.

Yuan, Y., Jiang, J., and Peng, T. 2010. “Corrosion process of steel bar in concrete in full lifetime,” *ACI Materials Journal*, 107(6), 562-567.

Zaiter, A., and Lau, T.L. 2021. “Experimental study of jacket height and reinforcement effects on seismic retrofitting of concrete columns,” *Structures*, 31, 1084-1095.

Zhang, C., Huang, W., Zhou, Y., and Luo, W. 2021. “Experimental and numerical investigation on seismic performance of retrofitted RC frame with sector lead viscoelastic damper,” *Journal of Building Engineering*, 44, 103218.

Table II1. Statistical properties for stochastic simulation

Variable	Mean	COV	Distribution	Reference
Geometry	Various	0.03	Normal	Okeil et al. (2002)
Concrete cover (C)	63.5 mm	0.2	Normal	Li and Melchers (2005)
Critical concentration (C_{cr})	0.4%	0.38	Normal	Val and Stewart (2003)
Equilibrium concentration (C_0)	1.6%	0.50	Lognormal	Stewart and Rosowsky (1998)
Diffusion coefficient (D_c)	1×10^{-8} cm^2/s	0.75	Lognormal	Stewart and Rosowsky (1998)
Water-to-cement ratio (w/c)	0.4	0.10	Normal	Fox et al. (2007)
Rebar diameter (ϕ_0)	12.7 mm	0.015	Normal	Nowak and Collins (2013)
Yield strength of steel (f_y)	414 MPa	0.025	Normal	Mirza et al. (1980)
Concrete strength (f'_c)	27 MPa	0.125	Normal	Nowak and Collins (2013)
Concrete crushing strain (ε_{cu})	0.003	0.15	Lognormal	Baji and Ronagh (2016)
Cross-sectional area of steel (A_s)	Various	0.015	Normal	Nowak and Collins (2013)
Pitting corrosion (a_{pit} and p_{pit})	Various	0.10	Normal	Kim et al. (2011)
Elastic modulus of CFRP (E_f)	124 GPa	0.20	Lognormal	Atadero and Karbhari (2008)
Cross-sectional area of CFRP (A_f)	32 mm^2	0.05	Lognormal	Atadero and Karbhari (2008)

[1 mm = 0.0394 in.; 1 cm^2 = 0.16 in.^{2}; 1 MPa = 145 psi; 1 GPa = 145 ksi]

Table II2. Test matrix [1 mm^2 = 0.0016 $in.^2$; 1 kN = 0.225 kips]

Identification	Resin	Corrosion time (years)	Cross-sectional area of steel (mm^2)	Ultimate load (kN)
P25	Polyester-silica	25	141	47.0
P50	Polyester-silica	50	129	45.2
P75	Polyester-silica	75	114	40.4
P100	Polyester-silica	100	99	38.6
U25	UHPC	25	141	40.5
U50	UHPC	50	129	38.5
U75	UHPC	75	114	37.6
U100	UHPC	100	99	37.3
G25	Geopolymer	25	141	38.5
G50	Geopolymer	50	129	38.3
G75	Geopolymer	75	114	33.8
G100	Geopolymer	100	99	32.3

Table II3. Proposed effective stress factor for cementitious resins

Resin type	Corrosion damage	Expected loss of cross-sectional area of steel reinforcement (ΔA_s)	Effective stress factor (Ω)
Polyester-silica	Moderate	0% ≤ loss < 10%	0.80
	Significant	10% ≤ loss < 20%	0.60
	Critical	30% ≤ loss	0.55
UHPC	Moderate	0% ≤ loss < 10%	0.45
	Significant	10% ≤ loss < 20%	0.45
	Critical	30% ≤ loss	0.45
Geopolymer	Moderate	0% ≤ loss < 10%	0.40
	Significant	10% ≤ loss < 20%	0.30
	Critical	30% ≤ loss	0.30

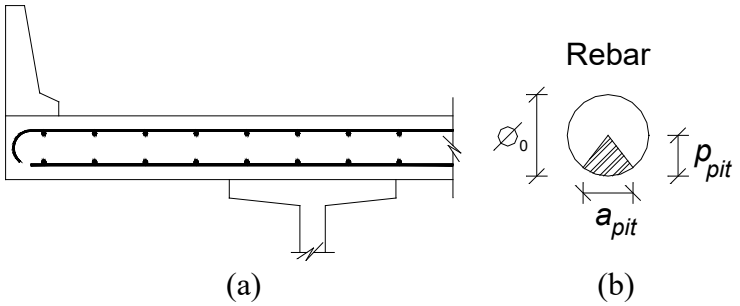

Figure II1. Corrosion damage: (a) benchmark bridge deck; (b) pitting corrosion

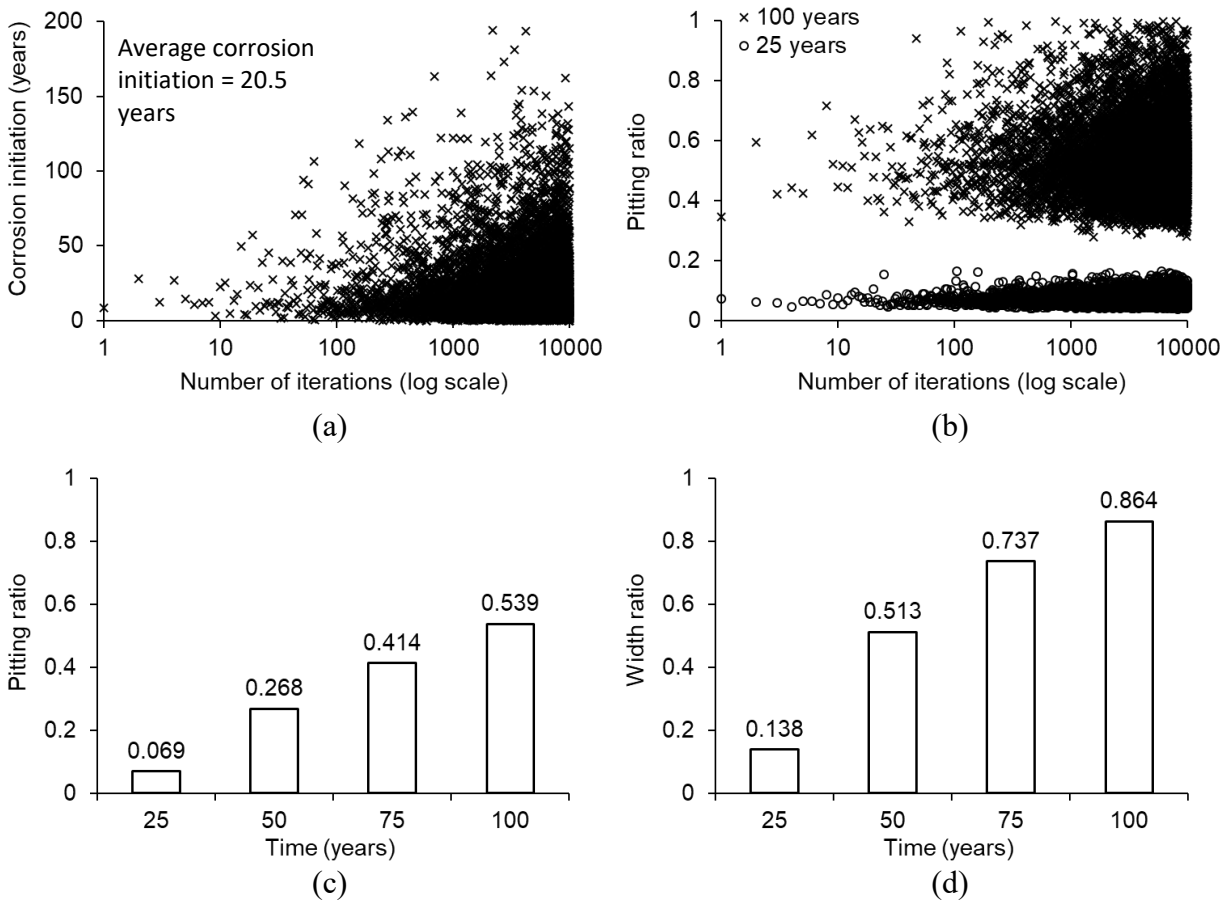

Figure II2. Corrosion damage of benchmark bridge deck: (a) simulated corrosion initiation year; (b) simulated pitting ratio; (c) average pitting ratio; (d) width ratio

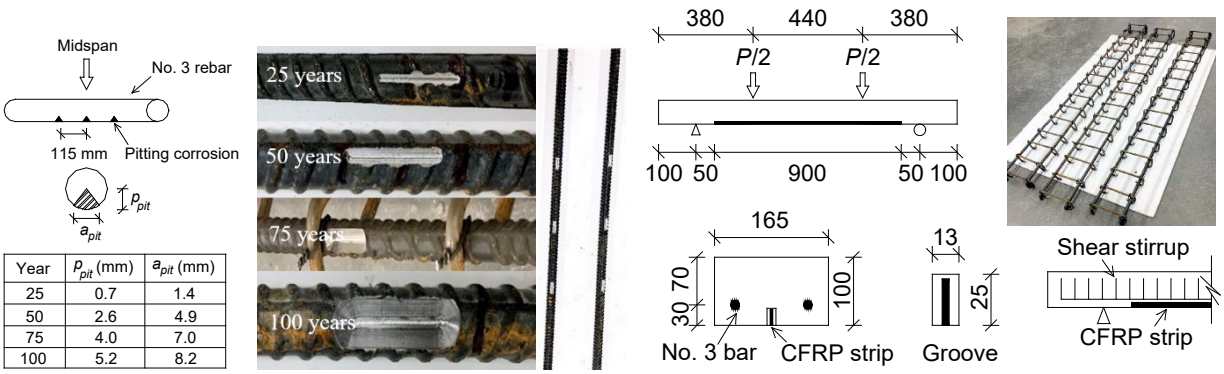

Year	p_{pit} (mm)	a_{pit} (mm)
25	0.7	1.4
50	2.6	4.9
75	4.0	7.0
100	5.2	8.2

(a) (b) (c)

[1 mm = 0.0394 in.]

Figure II3. Beam details (units in mm): (a) pitting corrosion; (b) simulated corrosion damage; (c) dimension

(a) (b) (c) (d)

Figure II4. Test methods: (a) concrete cylinder; (b) resin cube; (c) workability; (d) beam

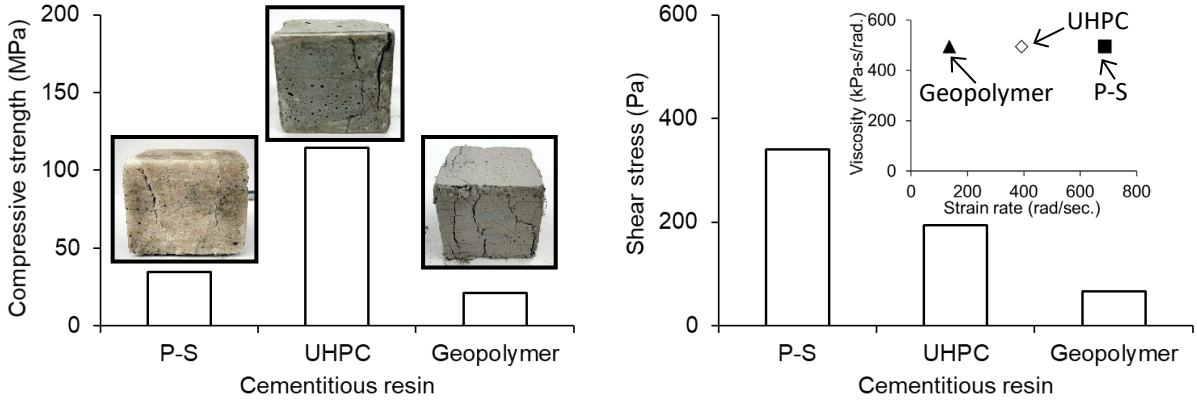

[1 MPa = 145 psi; 1 Pa = 0.02 lb/ft^2]

Figure II5. Properties of cementitious resins: (a) average compressive strength at 14 days of curing; (b) workability

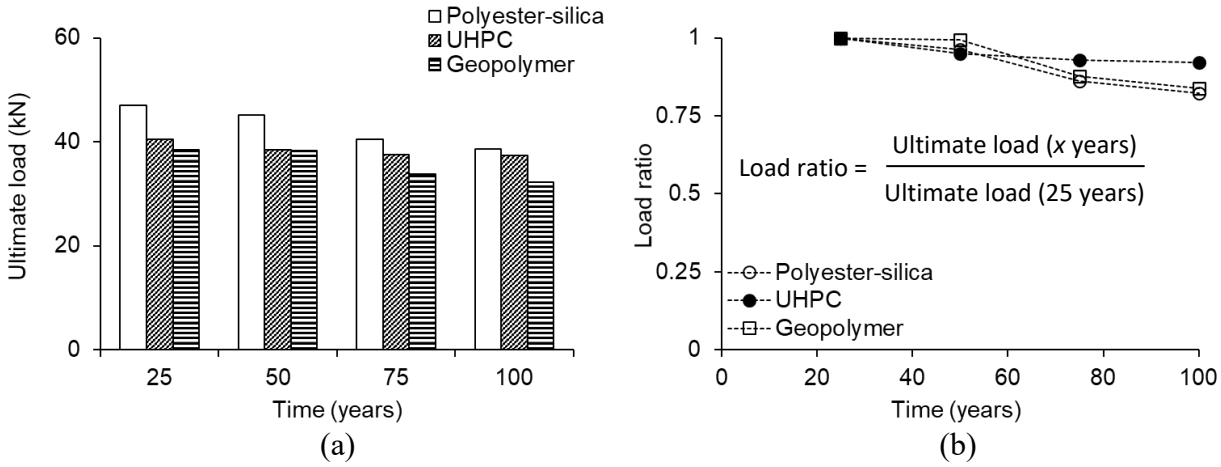

Figure II6. Flexural capacity of strengthened beams: (a) ultimate load; (d) load ratio

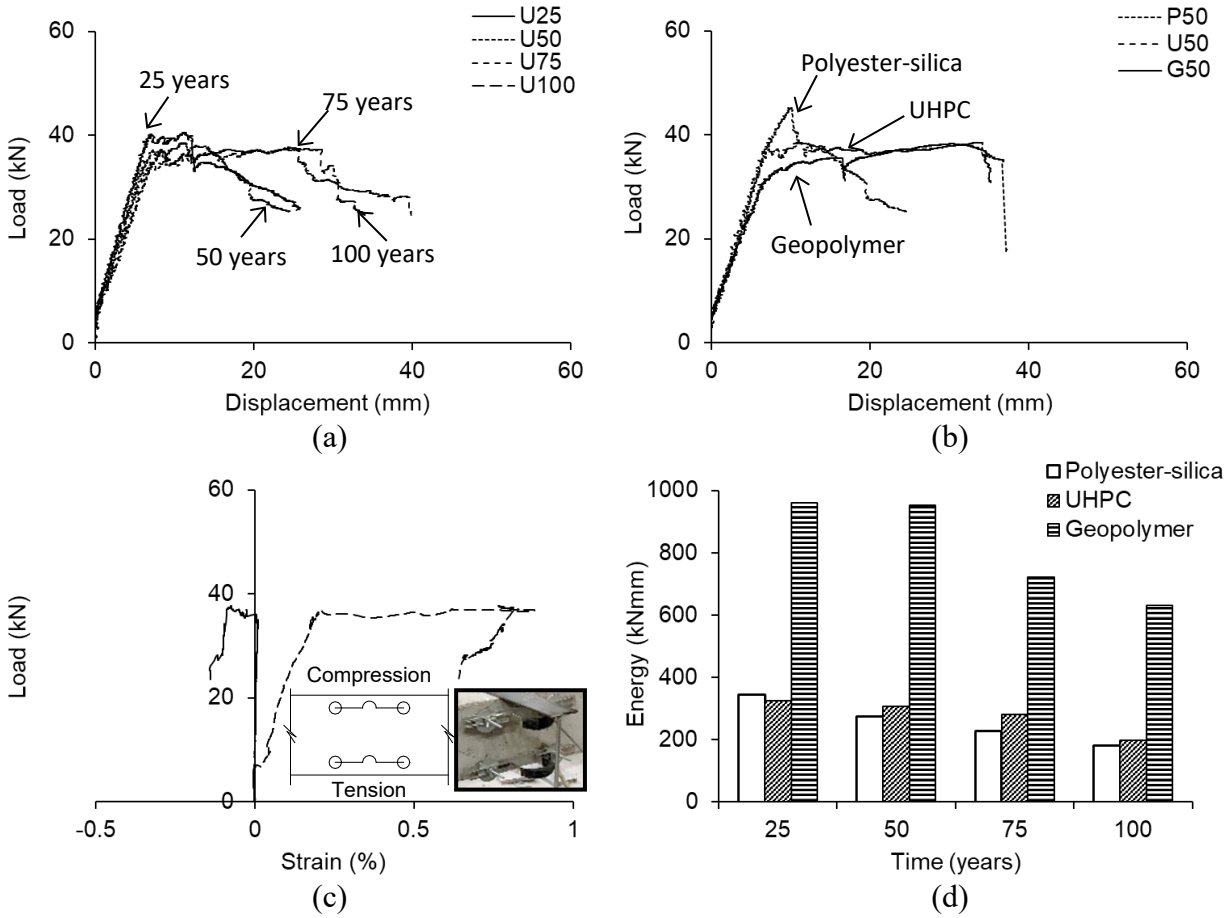

[1 kN = 0.225 kips; 1 mm = 0.0394 in.; 1 kNmm = 0.0089 kip- in.]

Figure II7. Flexural behavior: (a) load-displacement for UHPC; (b) comparison of load-displacement at 50 years; (c) strains of U75 beam; (d) energy dissipation

(a)

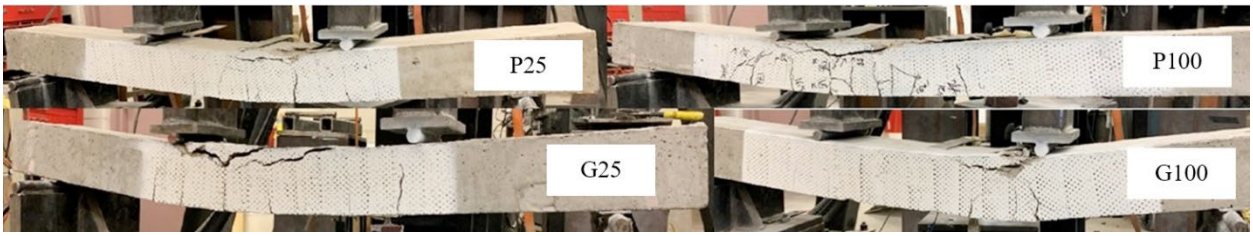

(b)

Figure II8. Failure mode: (a) beams with UHPC; (b) beams with polyester-silica and geopolymer

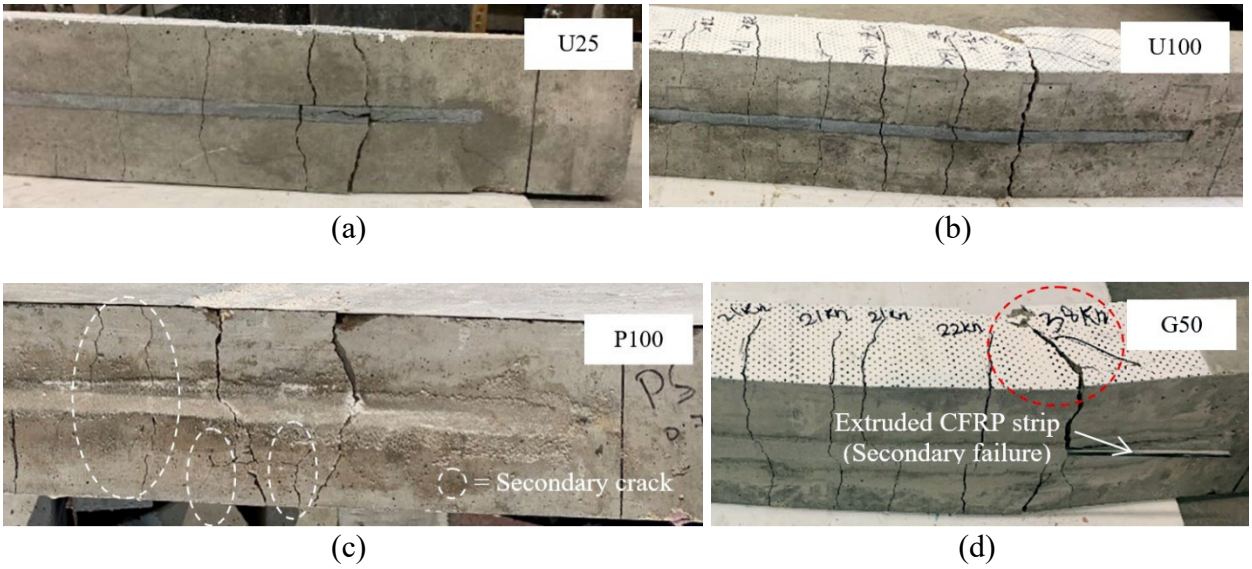

Figure II9. Interface between CFRP and substrate: (a) beam with UHPC at 25 years; (b) beam with UHPC at 100 years; (c) beam with polyester-silica at 100 years; (d) beam with geopolymer at 50 years

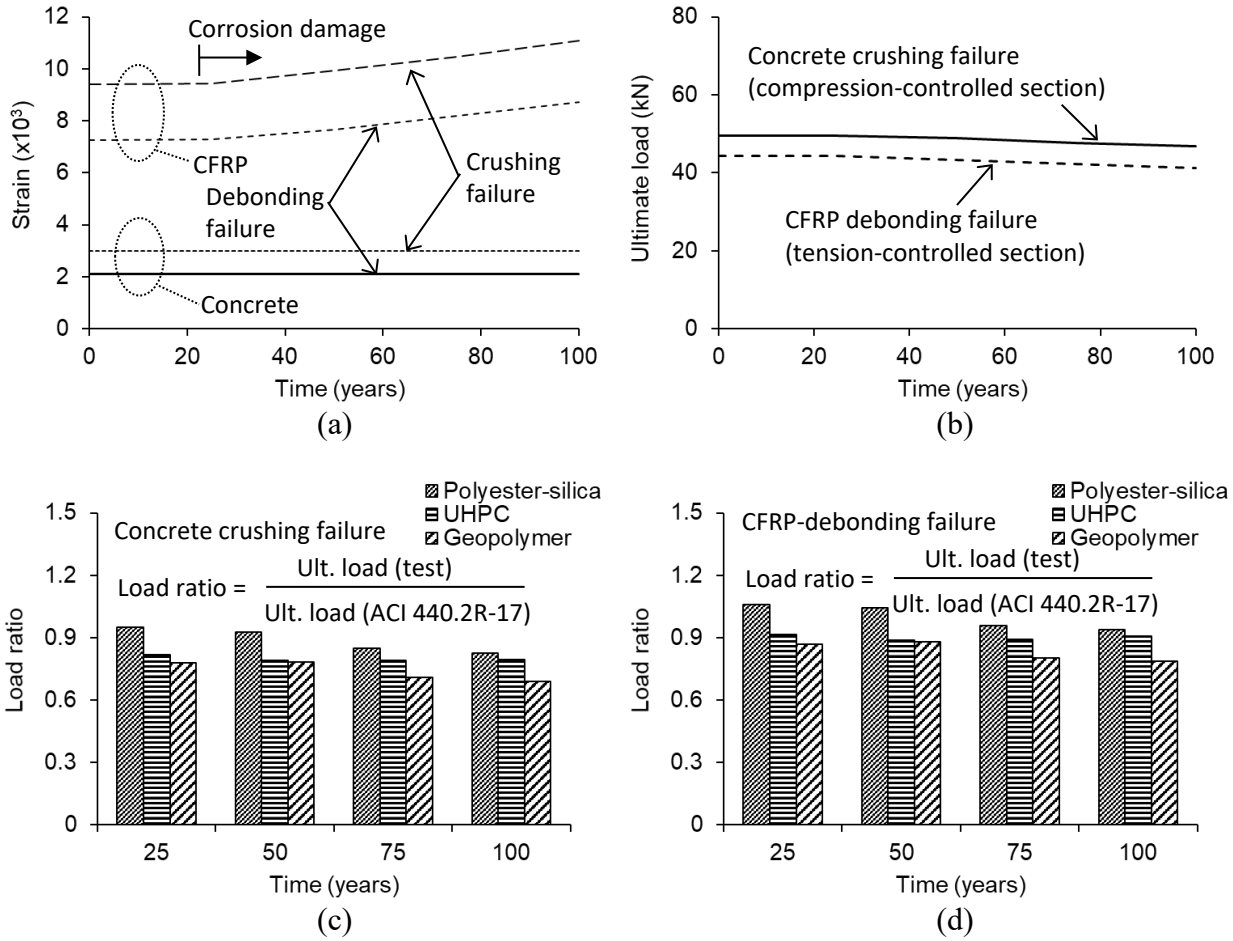

Figure II10. Assessment of bond performance: (a) calculated strains at failure based on ACI 440.2R-17 (ACI 2017); (b) capacity based on ACI 440.2R-17 (ACI 2017); (c) load ratio with compression-controlled section; (d) load ratio with tension-controlled section

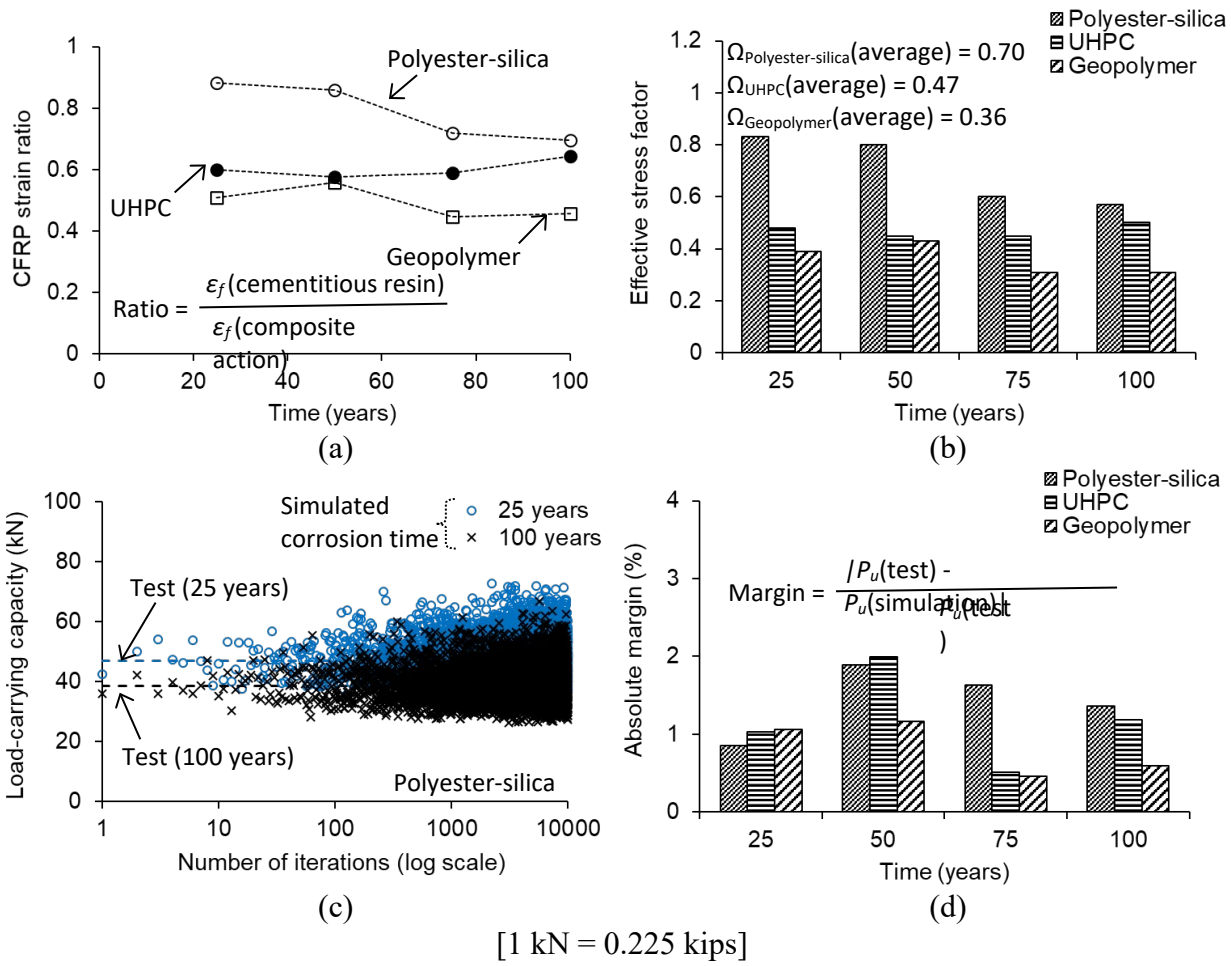

Figure II11. Bond efficiency of cementitious resins for NSM systems: (a) CFRP strain ratio; (b) effective stress factor; (c) simulated capacity vs. test capacity; (d) average absolute margin between test and simulation